

# Relationship between the contact force strength and numerical inaccuracies in piecewise-smooth systems

B. E. Saunders<sup>a</sup>, R. Vasconcellos<sup>b</sup>, R. J. Kuether<sup>c</sup>, and A. Abdelkefi<sup>a</sup>

<sup>a</sup>Department of Mechanical & Aerospace Engineering, New Mexico State University, Las Cruces, NM 88003, USA.

<sup>b</sup>São Paulo State University (UNESP), Campus of São João da Boa Vista, São João da Boa Vista 13876-750, Brazil.

<sup>c</sup>Sandia National Laboratories, Albuquerque, NM 87123, USA.

## Abstract

This work studies the different types of behavior and inaccuracies that can occur when contact is not adequately accounted for in a dynamical system with freeplay, as the strength of the contact stiffness increases. The MATLAB® *ode45* time integration solver, with the built-in Event Location capability, is first validated using past experimental data from a forced Duffing oscillator with freeplay. Next, numerical results utilizing event location are compared to results neglecting event location in order to highlight possible numerical errors and effects on multistable dynamical responses. Inaccuracies tend to occur in two different ways. First, neglecting event location can affect the boundaries between basins of attraction. Second, neglecting event location has little effect on the behaviors of the attractor solutions themselves besides merely resembling poorly converged solutions. Errors are less pronounced at the limits of soft or hard contact stiffness. This study shows the importance of accurately solving piecewise-smooth systems and the existing correlation between the strength of the contact force and possible numerical inaccuracies.

**Keywords:** Freeplay nonlinearity; event location; numerical accuracy; isolated resonances; multistable solutions

## 1 Introduction

Significant research has been performed in the field of non-smooth or discontinuous dynamical systems from both theoretical and applied points of view. This work includes understanding the behaviors unique to, and solution methods necessary for, non-smooth systems. For example, systems subject to friction or intermittent contact often experience discontinuity-induced bifurcations such as grazing and grazing-sliding bifurcations [1-4]. These behaviors are unique, do not occur in smooth systems, and oftentimes result in aperiodic or other complex responses [5-6]. Practically, non-smooth nonlinearities can also lead to premature wear and failure in parts [7] or cause undesirable noise [8]. Thus, when modeling the structural health or fatigue life of a non-smooth system, it is important to use analysis methods which can accurately and efficiently capture any and all non-smooth effects present in the system.

Freeplay contact is a particular type of non-smooth phenomenon characterized by a “dead zone” or gap between moving parts, within which no contact occurs. If the moving parts close this gap, then contact occurs between the parts. Freeplay is often modeled either as soft contact/impact, represented as a non-smoothness in a physical parameter such as damping or stiffness, or as hard impact, represented by an elastic restitution coefficient [9-10]. Examples of freeplay include contact between two gears due to backlash [8, 11-14] or between ball bearings [7], aeroelastic control surfaces [15-21], loosely supported structures [22-24], buildings in an earthquake [25-27], suspension systems [28], and self-propelling capsules to traverse pipes [29]. Newer fields include topics such as parameter identification [30] and contact-based control of systems [31]. This wide range of applicability means there is a lot of value in ensuring analysis methods can accurately and efficiently capture contact behaviors.

There has been a lot of development on methods to solve and analyze freeplay and other non-smooth systems. A brief overview of some numerical strategies is given here. The first is analytical methods, which have been used to study certain non-smooth nonlinearities. One technique is to utilize transformations, such as the saw-tooth time transformation used by Pilipchuk [32], when analyzing impact (i.e., hard contact). Here, the sawtooth function was used as the basis function for solutions to nonlinear vibro-impact systems. Mikhlin et al. [33] used the nonsmooth transformation approach to study the stability of a 2 degree of freedom vibro-impact absorber. Avramov et al. [34] studied a Duffing oscillator with impact using a non-smooth unfolding transformation. Pilipchuk [35] later extended non-smooth transformations to the analysis of rigid but inelastic vibro-impact oscillators. The closed-form solutions were able to describe non-stationary dynamics well. A recent review [36] covers further work on the topic of non-smooth transformations to analytically study vibro-impact systems, as well as describing the three most common styles: coordinate, state, and temporal transformations.

Mapping techniques have also been common for analytically studying non-smooth systems. Nordmark [37] introduced the discontinuity mapping to analyze grazing behavior in a pioneering work. This mapping was intended to be a local approximation near a grazing bifurcation. Grazing was found to cause a square-root singularity that leads to local, infinite stretching of phase space and result in complex responses. Nordmark [38] later introduced the limit mapping of an impact oscillator and used it to determine the system had three coexisting attractors. Molenaar et al. [39] studied an impact oscillator with soft/yielding impact and determined its grazing impact mapping. The authors found that the system displayed the same bifurcation behavior as a system with hard impact with only a change of the scale of the bifurcation parameter. Ma et al. [40] analytically, numerically, and experimentally studied four configurations of a soft impact oscillator and studied the system's Jacobian when

transitioning between non-impacting and impacting orbits. The behavior of the map far from grazing was also explored. They were limited to only studying period-1 orbits without increasing the number of equations to solve. Andreaus et al. [41] studied a forced bilinear oscillator using impact and return maps and found that many types of bifurcations and chaotic motion occur. Their solution technique involved numerically evaluating the transitions from non-contact to contact, but the mapping technique gave rise to "tedious and long" mathematical expressions required for the numerical code. Simpson et al. [42] compared the Nordmark mapping and Poincaré mapping of a soft impact oscillator and found the two mappings agreed to leading order. However, the Nordmark map was unable to detect narrow-band chaos or the presence of several large-amplitude attractors away from the grazing bifurcation. Fan et al. [28] studied the stick, non-stick, grazing, and periodic motions of a 2 degree of freedom (DOF) oscillator with soft contact analytically using G-functions, switching control laws, and mapping techniques, as well as numerically. Mappings have the advantage of not requiring additional computational work to precisely locate points of contact, but this is in exchange for oftentimes being approximations that are not always accurate away from the grazing bifurcations of interest.

Another method with a lot of attention recently is the use of nonlinear normal modes (NNMs), often combined with the harmonic balance method (HBM). Kuether et al. [43] have shown that NNMs can effectively capture complex behaviors such as isolated resonances that can exist in smooth nonlinear systems that are undamped and unforced. The authors calculated the NNMs of a cantilever beam with a nonlinear cubic spring to study the relationship with the damped, forced system response. Peter et al. [44] recently extended the use of NNMs to non-smooth systems by studying a beam with one-sided contact. A mixed shooting/harmonic balance technique was used to solve the finite element model and gave good agreement with experimental results. The technique also removed the need to define any contact parameters or impact law, along with the need to perform nonlinear system identification. Mikhlin et al. [33] had also used (NNM) theory in their analysis. The review by Renson et al. [45] covers recent advances in nonlinear modal analysis and computation. The combination of NNMs with HBM shows promise for reduced-order analysis of large-DOF systems. A common problem when using HBM, though, is that the non-smoothness of the contact force causes solver algorithms to fail. To resolve this issue, researchers often replace the piecewise function with a continuous and fully smooth function that closely approximates the piecewise function [24, 46, 47]. Other authors have shown that not all possible "regularization" functions may be appropriate to use, and that the choice of function is separate from the ability to actually capture contact behavior effectively [17, 48].

Probably the most common analysis method currently is direct numerical time integration using Runge-Kutta solvers [9, 12-14, 16-21, 31, 49]. There have also been a few modifications introduced in past decades to account for contact behavior. An early modification of classical solvers came from Henon [50], who introduced a modification based on the principle of piecewise time integration. The approach first proceeds with time integration and checks for a contact event on every timestep. After detecting that a discontinuity/contact boundary has been crossed, the method swaps the position and time as dependent/independent variables and reverse-integrates back to the exact location of the contact boundary in one step. Next, the values of the contact terms change as appropriate, and the regular time integration is restarted using the current position and velocity as new initial conditions (ICs). This method is also known as inverse interpolation. Using this approach, the exact piecewise representation of a contact term can be used, and no regularization is needed to represent the nonlinear force. Conner et al. [51] later showed that the classical, un-modified integration solvers can fail to accurately capture the effects of piecewise-smooth terms due to accumulating rounding error. Dai et al. [20] used the classical 4<sup>th</sup>-order Runge-Kutta method (RK4), incorporating Henon's method, to study chaos in an aeroelastic system with freeplay nonlinearity. They found that their RK4Henon method captured limit cycle oscillations and chaos as well as classical RK4 and a regularization using a rational polynomial, but RK4Henon was the only method to capture long-lived chaotic transient effects. Wayhs-Lopes et al. [52] discussed how numerous researchers consistently report accurate, computationally efficient results using Henon's method for aeroelastic systems. They also proposed a matrix notation for Henon's method in terms of generalized coordinates, and they obtained accurate results after extending Henon's method to discontinuities in velocity to study friction effects.

Alternatives to Henon's method include a "Newmark step-by-step iteration method" used by Andreus et al. [25] to study the response of buildings to impacts during an earthquake. Another is Runge-Kutta with a "method of successive approximations" to locate contacts, as used by Blazejczyk et al. [9]. The authors compared hard and soft impact models applied to the same vibro-impact systems. They found the results agreed well when the system had a stiff base, but the hard-impact model gave wrong results for an elastic base when the duration of body contact is non negligible.

There are some recent papers that make no mention of any specific method to accurately capture contact. Bazhenov et al [10] compared two impact models on a 2DOF vibro-impact system, based on hard and soft impact. They found both models give similar results in the case of elastic rigid impact, but the hard-impact model was unsuccessful at simulating the system with soft impact. The authors mention they use 4<sup>th</sup>-order Runge-Kutta to perform numerical integration but do not mention any contact technique. Brandão et al. [49] investigated a 4DOF Jeffcott rotor-stator system with

intermittent contact. The authors saw a rich variety of nonlinear behaviors. They employed a variable timestep 4<sup>th</sup>-order Runge-Kutta method. When the system transitions from non-contact to contact, the timestep is iteratively decreased until an error metric is satisfied. Brzeski et al. [31] also simply used a 4<sup>th</sup>-order Runge-Kutta method but with a fixed timestep. Wang et al. [11] used MATLAB® to solve for the dynamics of a railway vehicle gear system using Runge-Kutta of an unspecified order. Yang et al. [12] used a 5<sup>th</sup>-order method with a fixed timestep, while Chen et al. [14] stated they employed MATLAB® with a Runge-Kutta 5/6 method and variable timestep. Christopher et al. [27] used the MATLAB® ode15s solver to study a MDOF building structure impacting a rigid stop to simulate the effects of earthquake pounding. They regularized the contact force with a smooth sigmoid function. They found that the system response complexity increases with the contact-to-structure stiffness ratio. Suda et al. [6] showed the condition required to avoid large-amplitude chaotic oscillation in a soft-impact oscillator, which is dependent on the forcing frequency being at or near an integer multiple of the system's natural frequency. The divergence from period-1 to chaotic orbits is caused by coexisting saddle cycles converging onto the main orbit at the grazing parameter value. They obtained numerical results through "brute-force simulation", which likely implies time integration, but no further details are given. Other researchers make little to no mention of the numerical solver they use at all [4, 8, 13, 29].

There also exist several popular software packages used for nonlinear dynamical analysis, including AUTO [53], MATCONT [54], COCO [55], and MANLAB [56]. The latter three of these are based on MATLAB® to take advantage of its wide availability and ease of use. MANLAB, however, is designed for smooth systems. Chong et al. [57] used their own MATLAB® software package, ABESPOL, in parallel with COCO [55] to give a global overview of the dynamic behavior of a SDOF vibro-impact system with soft impact. They studied the effects of every system parameter (except gap size) and explored discontinuity-induced bifurcations with continuation. ABESPOL uses MATLAB® ode15s with its built-in Event Location capability [58]. Jiang et al. [59] also used the ABESPOL/COCO software package to study the differences between discontinuity-induced bifurcations in a vibro-impact system for both elastic and rigid impact. They also performed bifurcation analyses and found that smooth bifurcations transitioned into non-smooth bifurcations as the contact stiffness increases to hard/rigid impact.

There have been other studies performed using the MATLAB® ODE suite and its available Event Location capability to solve contact/impact problems. Calvo et al. [60, 61] have published papers and a software package (DISODE45) on the use of MATLAB® event location/detection (synonyms in this work) to solve piecewise-smooth, Filippov, and other non-smooth systems. Wright et al. [62] explored

the use of both MATLAB<sup>®</sup> ode45 and ode23 with event location to solve piecewise-smooth systems in particular. They found that the state event location is critical to accurately solving the equations of motion. The authors also discussed the relevant settings that can be set in MATLAB<sup>®</sup> to help improve result accuracy, along with the convergence and computational stability of solutions. Later, Dallas et al. [63] gave some guidelines for selecting a MATLAB<sup>®</sup> ODE solver and its parameters for hybrid stiff/non-stiff systems. The question of selecting the best solver for such a system was open, and they found ode45 and ode113 were among the best performing ODE solvers for most cases. Event detection was used and compared to code based on simple logic statements. Frumusa et al. [64] used MATLAB<sup>®</sup> with event location for numerical analysis of excessive backlash in an aircraft control surface.

An advantage of using time integration with event location in MATLAB<sup>®</sup> is the built-in functionality that can be adapted to solve many different nonlinear ordinary differential equations. However, the study of MATLAB<sup>®</sup> event location/detection applied to freeplay systems in particular seems to be lacking in the literature. There also appears to be, from a nonlinear dynamics point of view, little discussion on the effects of neglecting contact behavior in a numerical solver. With the widespread popularity of these MATLAB<sup>®</sup> based methods and solvers, and considering the number of cited works that make no mention of any procedure to accurately locate contact events, it may be particularly valuable to know how the lack of accurate event location can affect the dynamics of a contact system. This work therefore studies the different types of inaccuracies that can occur when contact behavior in a freeplay system is not adequately captured with an event location procedure. Particular focus is given to the effects of increasing the strength of the contact force stiffness to observe the effects of both soft and hard contact/impact on the system. A MATLAB<sup>®</sup>-based event location method, based on the work of Wright et al. [62], is first validated against experimental data and then used for subsequent simulations. Nonlinear dynamics features used in this analysis include frequency response curves, bifurcation diagrams, time histories, phase portraits, Poincaré maps, and largest Lyapunov exponents (LLE) computed using Wolf's algorithm [65].

The remainder of this paper is outlined as follows: Section 2 describes the physical system studied in this work, which was developed by deLangre et al. [66]. Section 3 then briefly describes the MATLAB<sup>®</sup>-based numerical method. In Section 4, the numerical method is validated against deLangre's experimental data [66], and the existence of multiple solutions is analyzed in more detail. Section 5 studies the importance of accounting for contact behavior as the freeplay contact stiffness increases in strength. Conclusions from the study are presented lastly in Section 6.

## 2 Problem formulation

The system considered in this study was the experimental system used by deLangre et al. [66]. They originally proposed this system in order to evaluate time integration techniques. This system was later used by Alcorta et al. [47] to study bifurcation tracking. Figure 1 gives a visual representation of the system. The physical system consisted of a heavy block, hollow on the inside and supported by two steel bars clamped to each side. The steel bars, when modeled as slender Euler-Bernoulli beams, give rise to a cubic-stiffness restoring force due to geometric nonlinearity. A magnet coil is attached to the block and is driven by applying a varying voltage to a magnetic coil in order to oscillate the block sinusoidally. Within the hollow of the block, there is a fixed rigid stop that is coincident with the equilibrium position of the block's center of mass. There are also two elastic springs, one on each side of the block in the direction of motion. Intermittent contact occurs whenever either spring hits the rigid stop. Gap sizes and stiffness could be changed by using different springs.

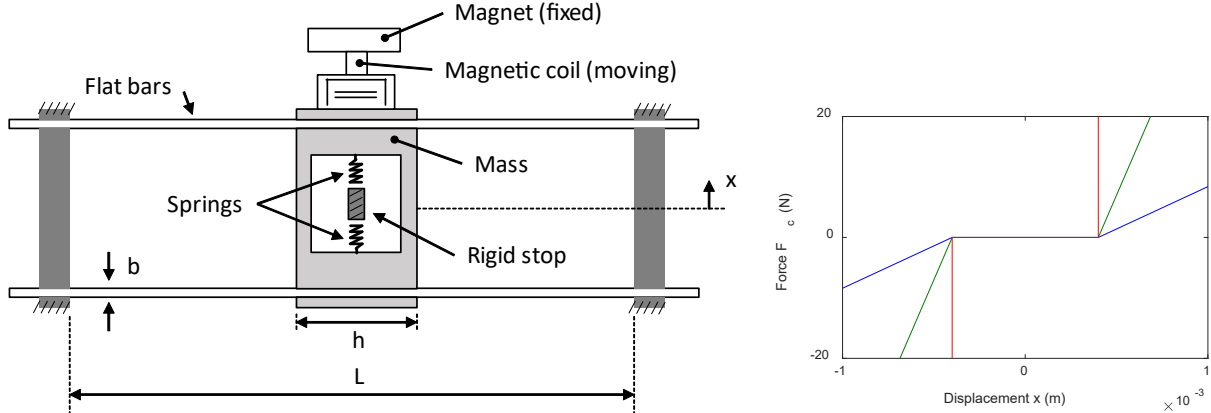


Fig. 1: Diagram of the experimental system from [66] studied in this paper, and a plot of contact force vs. displacement curves for increasing contact stiffness: the blue curve has contact stiffness  $K_c = 1.4 * 10^4 N/m$ , the green curve has  $K_c = 7.0 * 10^4 N/m$ , and red has  $K_c = 1.4 * 10^{10} N/m$ .

From Figure 1, this system can be modeled by the following single degree-of-freedom equation of motion [48]:

$$m\ddot{x}(t) + c\dot{x}(t) + kx(t) + \alpha x^3 + f_{NL,c}(x) = p\cos(\omega t) \quad (1)$$

where  $m$  denotes the effective mass of the system,  $c$  is the viscous damping,  $k$  represents the linear stiffness,  $\alpha$  is the nonlinear cubic stiffness of the support beams,  $f_{NL,c}$  denotes the freeplay force term,  $p$  is the nominal forcing magnitude, and  $\omega$  represents the forcing frequency. deLangre et al. [66] reported that, due to the electromagnetic field of the excitation, the force actually applied to the moving mass required a frequency-dependent correction, which they modeled in the following form:

$$p_{eff} = p \left( 1 - \frac{18}{\omega^2} \right) \quad (2)$$

where  $p_{eff}$  is the actual forcing magnitude and substitutes for  $p$  in equation (1). Rewriting equation (1) provides the new equation of motion:

$$\ddot{x}(t) + 2\zeta\omega_n\dot{x}(t) + \omega_n^2x(t) + \frac{\alpha}{m}x^3 + \frac{1}{m}f_{NL,c}(x) = \frac{p_{eff}}{m}\cos(\omega t) \quad (3)$$

The freeplay force term can be represented as:

$$f_{NL,c}(x) = \begin{cases} K_c(x + j_1), & x < -j_1 \\ 0, & -j_1 \leq x \leq j_2 \\ K_c(x - j_2), & x > j_2 \end{cases} \quad (4)$$

where  $K_c$  is the stiffness of both of the contact springs, and  $j_1, j_2$  are the respective lower and upper spring gap boundaries. deLangre et al. [66] noted that contact dissipation was negligible compared to modal dissipation, so there is no piecewise-smooth damping term to accompany the stiffness term. Further, forcing term  $f_{NL,c}$  only contributes to the equation of motion whenever the displacement exceeds  $x = -j_1$  or  $x = j_2$ . deLangre et al. [66] used a consistent set of parameter values when generating numerical results, as listed in Table 1. The same values are used in the current study, although deLangre's original frequency range of 8-18 Hz is expanded to 2-30 Hz to explore a wider frequency band of responses.

Table 1: Parameters used by deLangre et al. [66].

Term	Description	Value
$m$	Total mass	3 kg
$\omega_n$	System natural frequency	5 Hz ( $10\pi$ rad/s)
$K$	Linear stiffness	$m\omega_n^2$ N/m ( $300\pi^2$ N/m)
$\zeta$	Modal damping	0.03
$\alpha$	Cubic stiffness	$7 * 10^8$ N/m <sup>3</sup>
$K_c$	Contact spring stiffness	$1.4 * 10^4$ N/m
$\omega$	Forcing frequency	2 – 30 Hz ( $4\pi$ – $60\pi$ rad/s)
$p$	Reference (nominal) external forcing level	1.5 and 4 N
$j_1, j_2$	Lower, upper spring boundaries	[0.4, 0.4], [0, 0.4], and [0, 0.8] mm

### 3 Methodology: numerical integration with event location/detection

The numerical method used in this work is based on the MATLAB<sup>®</sup> *ode45* time integration solver, and it utilizes the optional Event Location capability [58]. This section gives a brief overview of how this method works. For more detail on the relevant MATLAB<sup>®</sup> functions and settings, the reader is referred to the paper by Wright et al. [62]. In order to implement event location/detection, an *Events* function must be defined, which is a mathematical expression describing the positions where contacts will happen. When a timestep crosses a contact boundary, the events function changes sign and the root-finding *odezero* function is employed to precisely locate the time of the event. *Odezero* uses the Illinois method, an optimized variant of the *regula falsi* root-finding method, to locate the event [67].

This forces a timestep to occur at the contact event, avoiding the inaccuracy that comes with abruptly time-stepping through a discontinuity/contact boundary. A while loop is then used to restart the integration at this point, using the current states as initial conditions. The time integration is restarted and continues until the next event is detected, and this process is repeated for the desired total timespan in the while loop. For comparison, event location's root-finder replaces the step in Henon's method [50] in which the solution is reverse-integrated in time back to the exact position of a contact in a single timestep. This event-driven integration scheme can improve simulation accuracy in nonlinear systems with initial condition sensitivity, multistable solutions, and chaotic motion. Figure 2(a) shows an example of this procedure; the time history starts in the region  $x > j_2$  (red region), stops and restarts before entering the region  $-j_1 \leq x \leq j_2$  (green region), and stops and restarts before entering the region  $x < -j_1$  (blue region), etc. Also note that *ode45* uses an adaptive timestep, so it often reduces the step size near the contact boundaries. A disadvantage to this numerical method is that, as a direct time integration method, unstable responses cannot be computed; only stable responses can be found.

In the physical system of interest in equations (3) and (4), contact occurs whenever the displacement reaches  $x = -j_1$  or  $x = j_2$ . Figure 2(b) shows a time history and the first few contact events for a simulated forced response. Table 2 shows that, upon terminating the time integration at the marked events in Figure 2(b), the absolute difference between the current position  $x(t)$  and the corresponding contact boundary is on the order of  $10^{-16}$ - $10^{-18}$  m. This accuracy is 12 to 15 orders of magnitude lower than the scale of the system's oscillation, which is on the order of  $10^{-3}$  to  $10^{-4}$  m, and is near the order of machine precision. This implies that the event detection accurately, within a few orders of magnitude of machine precision, resolves the time at which contacts/impacts occur. This should ensure, especially for a chaotic response, that there is minimal numerical error added beyond what is already present from machine rounding.

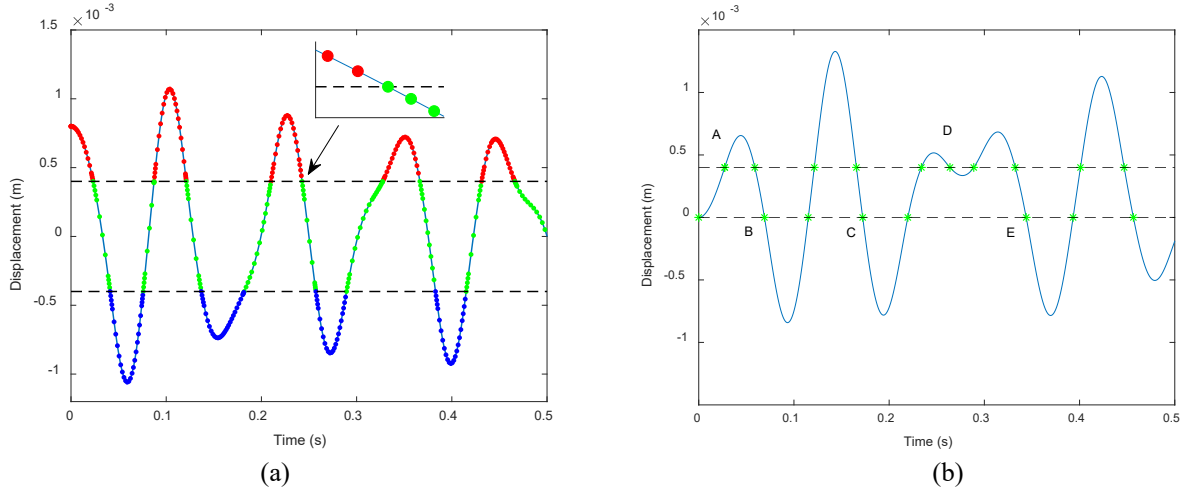


Fig. 2: (a) Time history that visualizes the event location/switching procedure. Red, green, and blue colors indicate time points beyond the upper freeplay boundary, within the freeplay boundaries, and beyond the lower freeplay boundary, respectively. The inset is a zoom near one of the switchings from no-contact to contact to show a time point has been placed precisely at the freeplay boundary. (b) Time history showing the first few instances of contact events marked with green dots. Information about the dots labeled A-E appears later in Table 2.

Table 2: Absolute differences in contact event positions from their respective freeplay boundaries, for the marked events in Figure 2(b)

Marker	Time (s)	Position (m)	Absolute difference, $\times 10^{-16} m$
A	0.0272825817630530	4.000000000000050E-04	0.051499603193060
B	0.0690283299748320	-4.095573706563990E-17	0.409557370656400
C	0.1722049632988320	-1.045645232726480E-16	1.045645232726490
D	0.2638692359706180	3.99999999999690E-04	0.308997619158370
E	0.3439311311853270	-1.436567878543290E-16	1.436567878543290

#### 4 Numerical validation of time-integration scheme

In this section, the event detection numerical method based on the work of Wright et al. [62] is validated against experimental data from deLangre et al. [66]. MATLAB<sup>®</sup> settings believed to be best for this system are used, including extremely tight tolerances to ensure the solution is well-converged. All six FRC plots from deLangre’s experiments [66] include results from three different spacing gaps ( $j_1, j_2 = [0.4, 0.4], [0, 0.4], \& [0, 0.8]$  mm, cases a, b, and c, respectively) and two forcing amplitudes ( $p = 1.5 \& 4 N$ ). Each case is labeled by its gap type and forcing. For example, the low-asymmetry, high forcing case is denoted by “asymmetric case b4”. These combinations are presented in Figure 3 and compared to numerical results. The frequency response curves, which show the steady-state root mean square (rms) solution amplitude as a function of forcing frequency, are computed using multiple initial conditions at each forcing frequency value to reveal the presence of multiple solutions. Multiple solutions at a given forcing frequency show up as multiple branches in the figure, and chaos appears as erratically spaced dots. The parameter values from Table 1 are used for each of the six plots, with

ode45 tolerances of  $RelTol = 10^{-12}$  and  $AbsTol = 10^{-12}$  and all other available ode45 options default. All plots on the left are at forcing  $p = 1.5 N$ , and the right plots are at forcing  $p = 4 N$ .

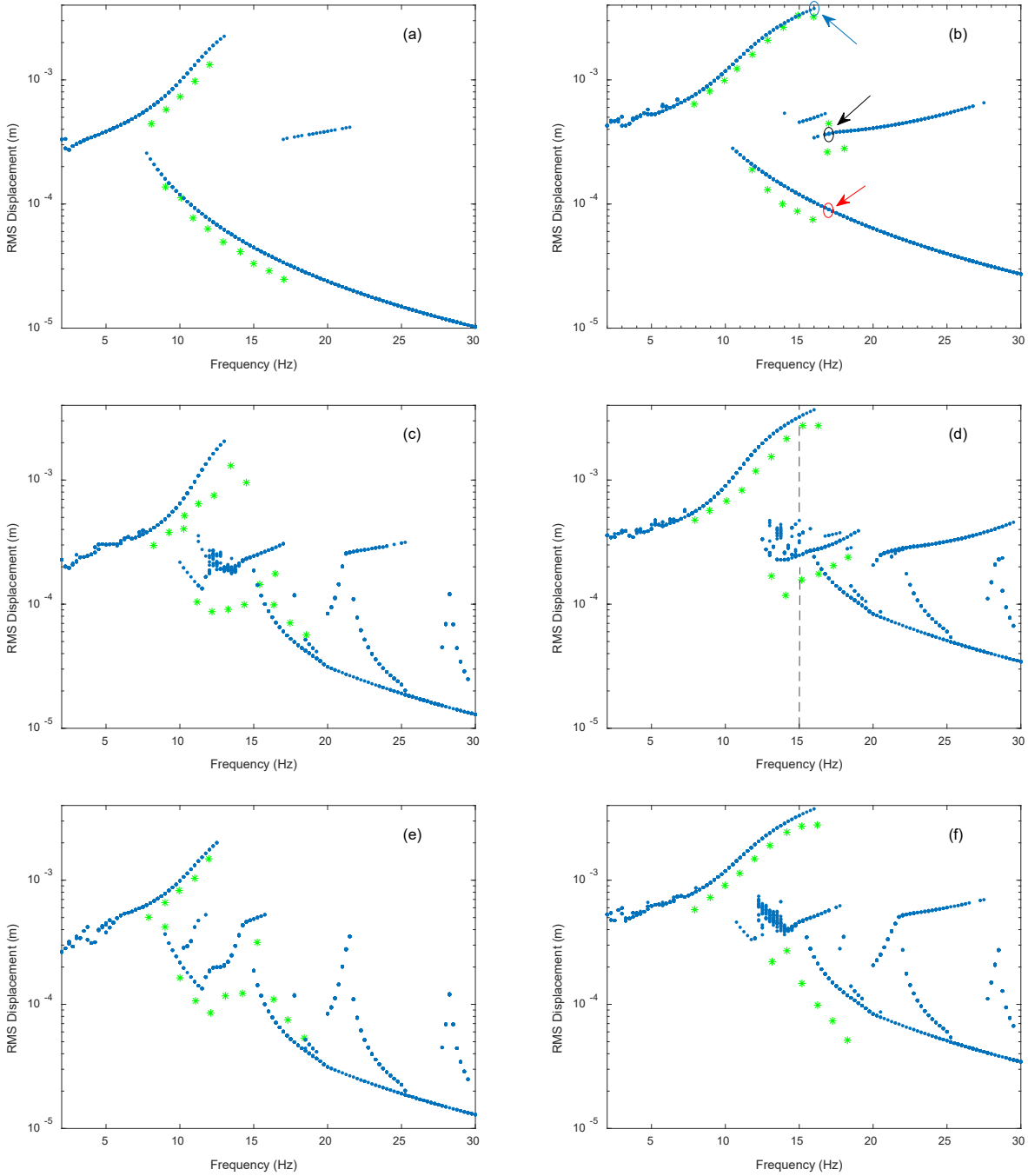


Fig. 3 Frequency response curves, comparing numerical results using event location (blue dots) versus deLangre's experimental data [66] (green dots). Plots (a, b) have symmetric freeplay boundaries  $j_1 = 0.4 mm, j_2 = 0.4 mm$ , plots (c, d) have low asymmetry boundaries  $j_1 = 0 mm, j_2 = 0.4 mm$ , and plots (e, f) have high asymmetry boundaries  $j_1 = 0 mm, j_2 = 0.8 mm$ . Plots (a, c, e) have forcing magnitude  $p = 1.5 N$ , and plots (b, d, f) have  $p = 4 N$ . The color-coded circles and arrows in plot (b) correspond to individual responses examined later in Figure 4. The dashed line in plot (d) denotes forcing frequency  $\omega = 15 Hz$ , at which there are multiple responses examined later in Figure 5.

As shown in Figure 3, the experimental frequency response curves step up and back down from 8 to 18 Hz. Although there was a fairly limited amount of experimental data, and notwithstanding any sources of experimental error that cannot be accounted for, the trend of the numerical results generally matches the available data well. The numerical responses on the upper branch, leading to the primary resonance peak, seem to generally overestimate the experimental results to some extent. There is no consistent over- or under-estimation for the lower branch. The region of largest discrepancy is for the asymmetric cases around forcing frequency  $\omega = 11 - 15 \text{ Hz}$ , in the area between the upper and lower branches. The frequency response is fairly widespread and erratic here, and there are multiple distinct values present at each frequency due to change in the initial conditions. Time histories indicate the system response has both period-adding and chaotic behaviors in this region.

For the asymmetric cases, there are also subharmonic resonance structures visible around  $\omega = 19 - 25 \text{ Hz}$  which generally seem to connect at their peaks to another branch that extends to higher frequencies. Similar structures were seen by Alcorta et al. [47] and are attributed to the contact-spring asymmetry. The cubic-stiffness nonlinearity in the system should produce a 3<sup>rd</sup>-order subharmonic resonance, defined as a resonance near  $\omega \approx 3\omega_n = 15\text{Hz}$ , and there is in fact a visible peak there in several of the FRCs.

Observing the symmetric cases, an isolated subharmonic resonance branch appears at higher frequencies for both forcing values, whose frequency band increases as forcing amplitude increases. For the strong forcing case a4, three experimental data points near 18 Hz are seen to lie on this isolated branch. It seems the numerical result is able to resolve more points along the stable portion of the isolated resonance branch. Researchers have typically found isolated resonances to be difficult to detect using continuation techniques, since they are disconnected from the branches that are initialized from low-level solutions approximated by a linearized system. More advanced techniques, such as nonlinear normal modes, have been studied for detecting isolated resonances [43].

To further explore the isolated resonance, Figure 4 shows time histories and phase diagrams for symmetric case a4 at 16 and 17 Hz for different initial conditions (see the circled responses in Figure 3(b)). When stepping up in frequency from 16 to 17 Hz, the oscillation can drop in amplitude from the blue curve (16 Hz) to either the red curve (17 Hz low) or the black curve (17 Hz high), depending on the position at the time of the frequency change. The red curve is in a low-amplitude response regime with no contact occurring, and it is also period-1. The black-curve response, however, lies on the isolated branch and is period-3. This is a clear result of the contact/freeplay nonlinearity on the system, since the only difference is the initial condition.

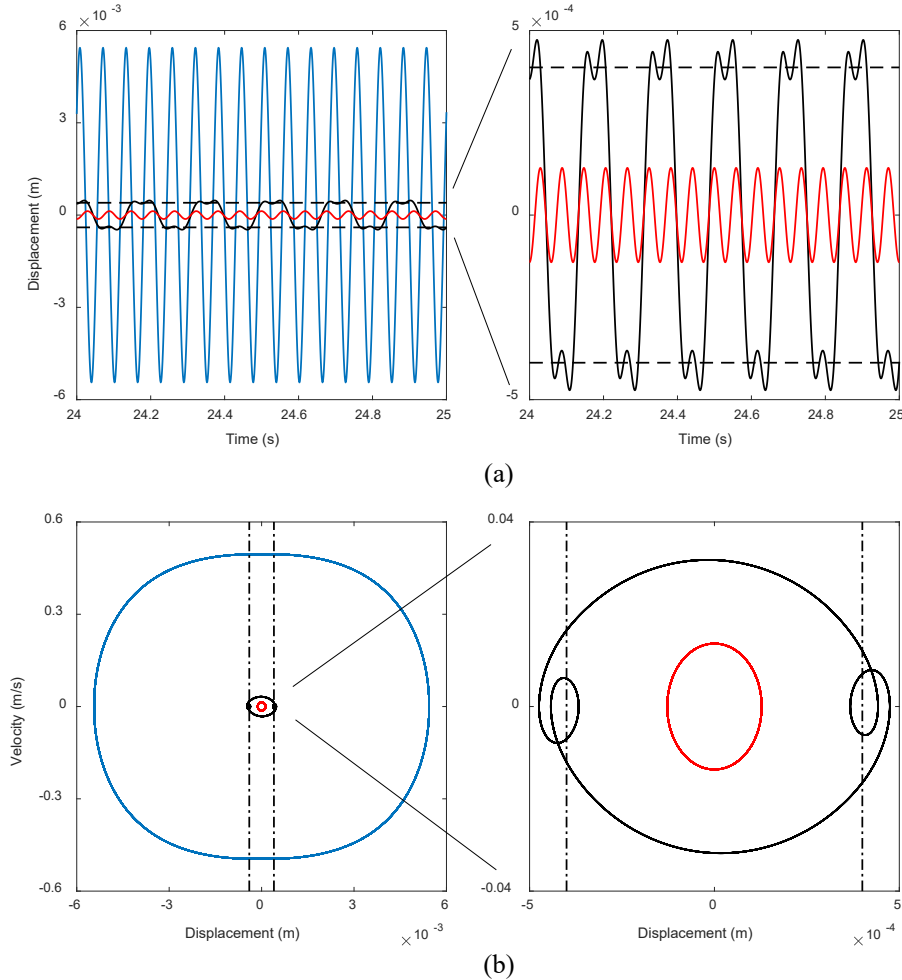


Fig. 4: (a) Time histories of symmetric case a4 ( $p = 4 \text{ N}$ ,  $j_1 = j_2 = 0.4 \text{ mm}$ ) showing two possible solutions when stepping up from  $\omega = 16 \text{ Hz}$  to  $\omega = 17 \text{ Hz}$ . (b) Phase portrait diagrams corresponding to the time histories. The curve colors correspond to the responses circled in Figure 3(b). Namely, the blue curves indicate the response at  $\omega = 16 \text{ Hz}$ , the black curves indicate the larger response at  $\omega = 17 \text{ Hz}$ , and the red curves indicate the smaller response at  $\omega = 17 \text{ Hz}$ . Dashed lines indicate the freeplay boundaries.

#### 4.1 Existence of multiple solutions and basins of attraction

The frequency response curves, created using a set of multiple initial conditions, very clearly show the presence of subharmonic and other isolated resonance branches. These results indicate the freeplay nonlinearity causes multistability, i.e. the presence of multiple possible stable solutions, over different frequency ranges. For example, for asymmetric case b4, there are five different response points visible at  $\omega = 15 \text{ Hz}$  (see the dashed line in Figure 3(d)). The steady-state time histories, phase portraits, and Poincaré maps (red dots) for the four lowest-amplitude responses are presented in Figure 5. According to Marzouk et al. [68], a period- $n$  response produces a Poincaré map with  $n$  points, a quasi-periodic response shows up as infinite points on a closed curve, and a chaotic response shows up as infinite points not on a closed curve but within a finite area. These results highlight how the responses are not

chaotic, but that they do have higher periods (3T, 5T, 12T, and 4T, left-right top-bottom, for  $T = 1/15$  s the forcing period) and are dependent on the initial conditions.

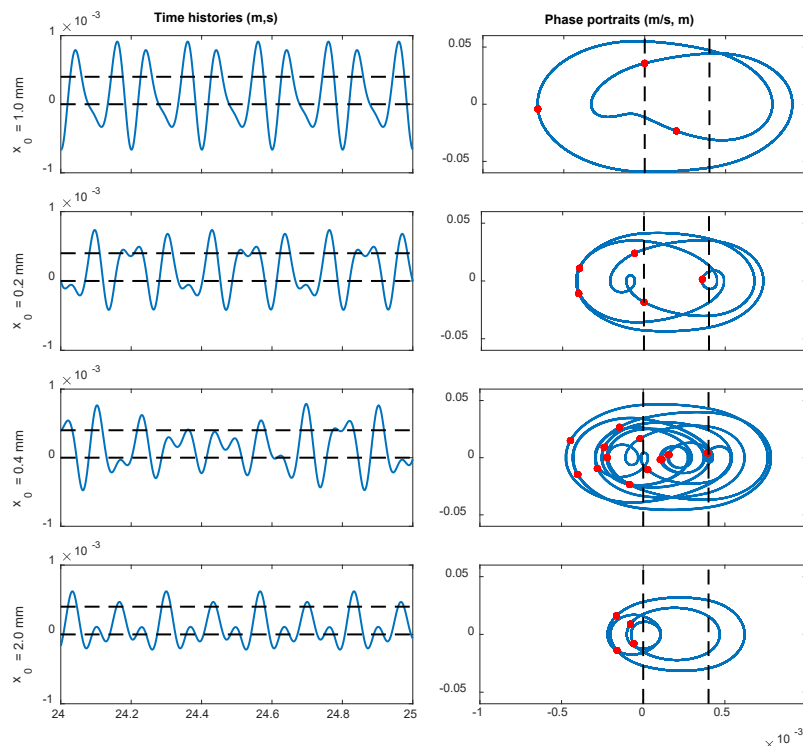


Fig. 5: The steady-state time histories (left) and phase portraits (right) with Poincaré maps (red dots) for asymmetric case b4 ( $p = 4$  N,  $j_1 = 0$  mm,  $j_2 = 0.4$  mm) at  $\omega = 15$  Hz for initial conditions  $x_0 = 1.0, 0.2, 0.4, 2.0$  mm. These correspond to the four lowest-amplitude responses at  $\omega = 15$  Hz in Figure 3(d).

The multistable behavior is analyzed further in Figure 6, which shows the basins of attraction for asymmetric case b4 at forcing frequencies of (1) 14.75 Hz, (b) 15 Hz, (c) 15.75 Hz, and (d) 16.5 Hz. This frequency band ranges around where the first prominent subharmonic resonance branch forms in Figure 3(d). The color corresponds to the steady-state peak amplitude according to the colorbar, and in all figures the large red swirl is corresponds to the highest-amplitude, primary resonance solution. The system transitions from three to four to two to three lower-amplitude solutions as the forcing frequency increases, all of which show a fine swirling structure with a significant amount of granularity. Another transition is from roughly equally dominating lower-amplitude solutions to one or two lower-amplitude solutions being dominant. Also, initial displacements near or within the freeplay boundary are not attracted to the high-amplitude solution unless they have a large initial velocity.

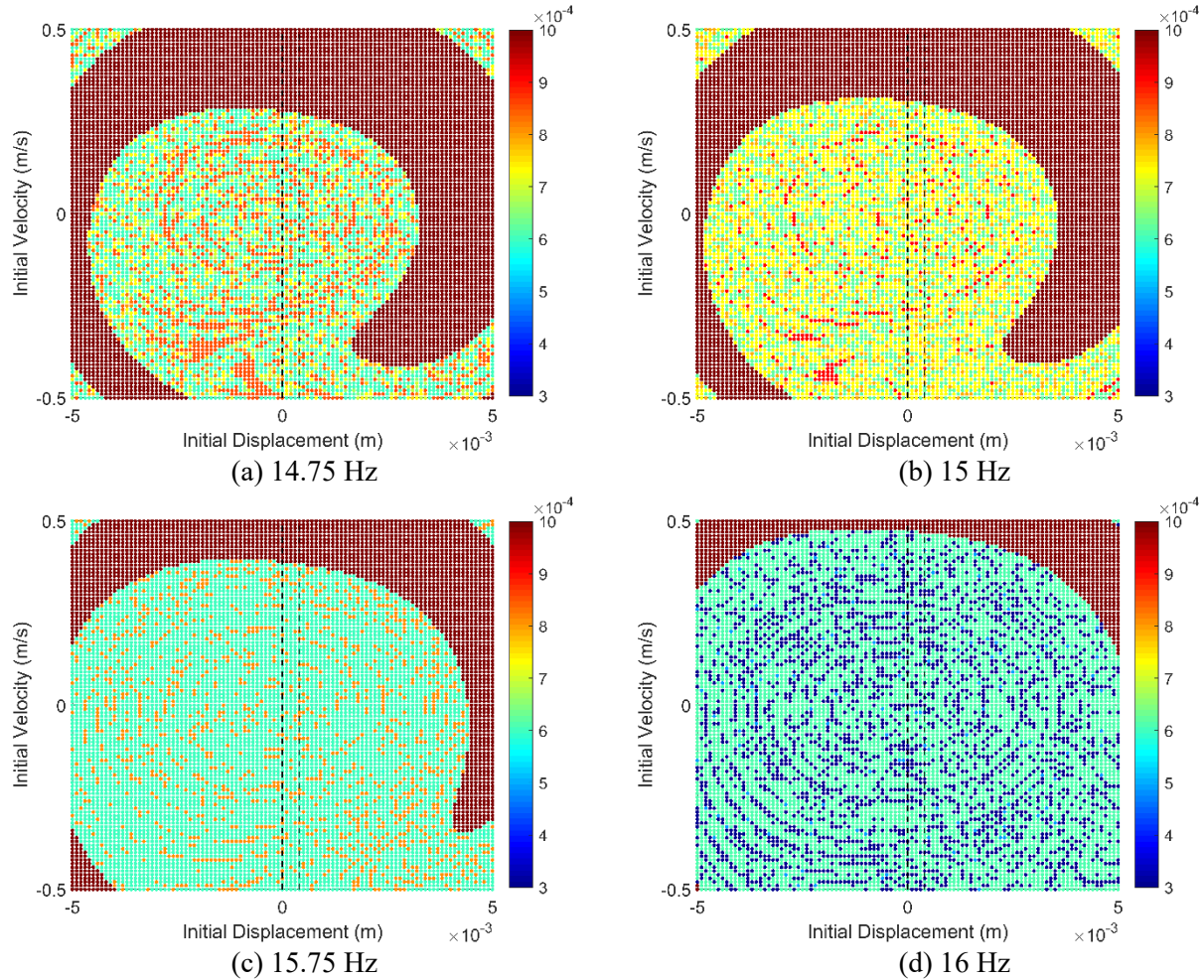


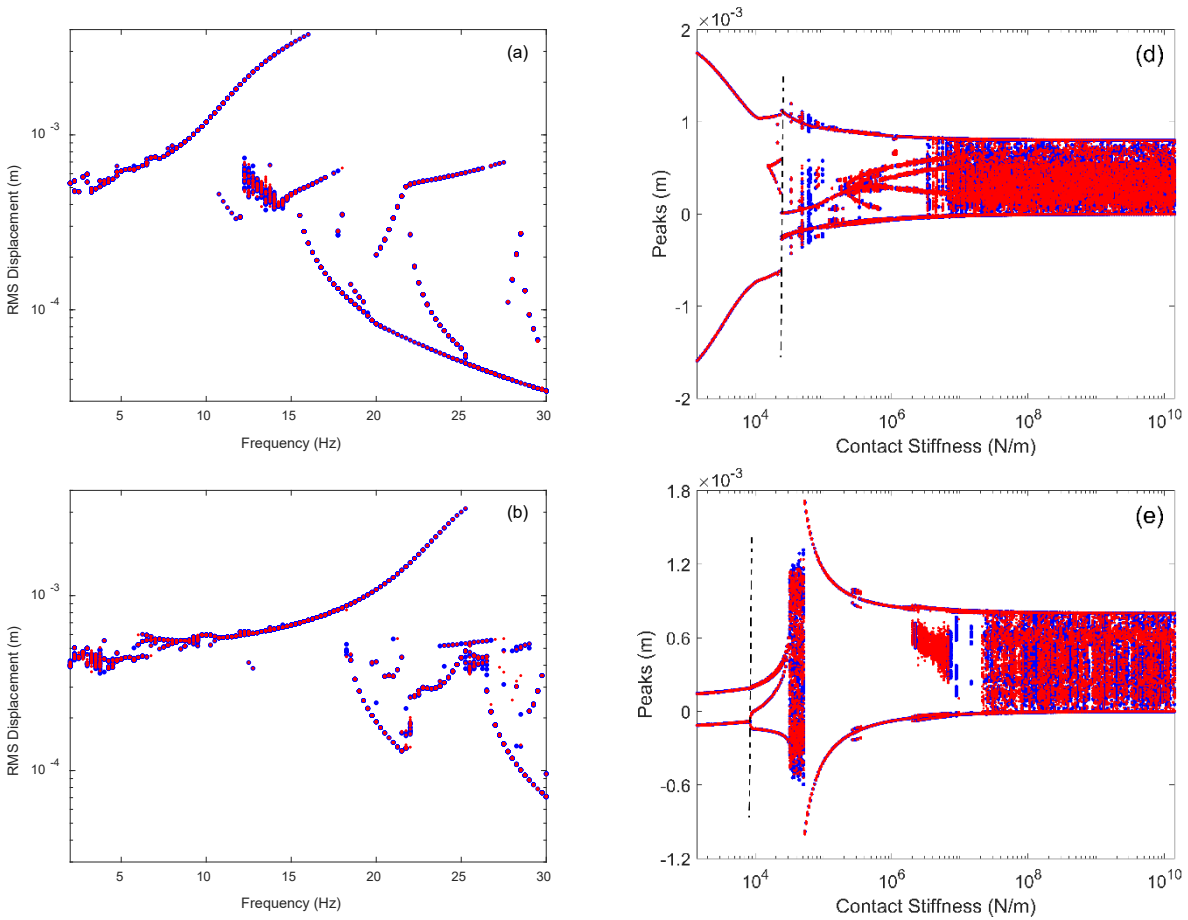
Fig. 6: Basins of attraction for asymmetric case b4 ( $p = 4 N, j_1 = 0 \text{ mm}, j_2 = 0.4 \text{ mm}$ ) at forcing frequencies  $\omega =$  (a) 14.75 Hz, (b) 15 Hz, (c) 15.75 Hz, and (d) 16 Hz. Color corresponds to steady-state peak amplitude according to the colorbars and is used to distinguish the different possible responses. The black dashed lines denote the freeplay boundaries.

The irregular and granular nature of the basins of attraction indicate a strong sensitivity to the initial conditions, which has practical implications for the modeling and testing of the dynamical system. The accumulating roundoff error that occurs when contact is not adequately located means that the shape of these basins may be incorrectly predicted and thus change the likelihood of an arbitrary initial condition converging onto any specific attractor. Any such statistical analysis is outside the scope of this work, but there exist ways of quantifying the size and extent of basins of attraction [69].

## 5 Importance of event detection for freeplay-based systems

In this section, numerical results including and neglecting accurate event location are compared. The objective is to highlight changes in the solutions or their basins of attraction that can occur due to inadequately capturing contact events. For the remainder of the paper, the system configuration used is the strong-forcing, high-asymmetry case c4:  $p = 4 N, j_1 = 0 \text{ mm}, j_2 = 0.8 \text{ mm}$ . MATLAB<sup>®</sup> ode45

tolerances of  $RelTol = 10^{-4}$  and  $AbsTol = 10^{-7}$  are used. The first results shown are frequency response curves (FRC) and bifurcation diagrams (BD) in Figure 7. The frequency response curves show the change in system response as the contact stiffness is increased from a relatively soft value of  $1.4 \times 10^4 \text{ N/m}$  to a medium and then a hard value of  $7.0 \times 10^4 \text{ N/m}$  and  $1.4 \times 10^{10} \text{ N/m}$ , respectively. Simulations with the initial displacement outside the gap region (i.e. for preloaded cases) have a much higher computational cost than un-loaded cases. Thus, for the hard-contact case, only small ICs within the gap are used to compute frequency response curves. The bifurcation diagrams show the points of zero velocity (peaks, valleys, inflections) of the steady-state response, for a single IC, as contact stiffness steadily increases towards hard impact.



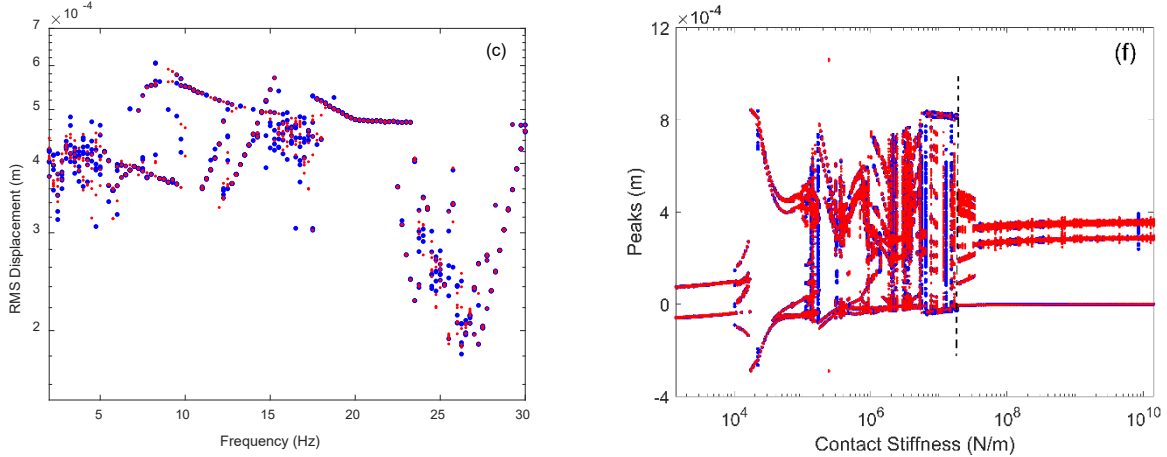


Fig. 7: (a, b, c) Frequency response curves and (d, e, f) bifurcation diagrams showing the effect of increasing contact stiffness on the system response. Plot (a) was created with a contact stiffness of  $K_c = 1.4 * 10^4 N/m$ , plot (b) has  $K_c = 7.0 * 10^4 N/m$ , and plot (c) has  $K_c = 1.4 * 10^{10} N/m$ . Plot (d) was created with a forcing frequency and initial displacement of  $w = 5 Hz, x_0 = 0.32 mm$ , plot (e) has  $w = 17 Hz, x_0 = 0.32 mm$ , and plot (f) has  $w = 23 Hz, x_0 = 0.32 mm$ . All plots had  $p = 4 N, j_1 = 0 mm, j_2 = 0.8 mm$ . The blue dots indicate results obtained using event location, and red dots indicate without event location. Blue dots are slightly larger to show overlap. The black dashed lines in plots (d-f) indicate bifurcations studied later in Sections 5.1-5.3.

Figure 7(a) compares the system's FRC for soft contact, given initial displacements  $x_0 \in \{0, \pm[0.1, 0.2, 0.4, 0.8, 1, 2, 3, 4, 5]\} mm$ , when event location is off and on. It is evident that there is only slight visual difference between the two curves, and mainly in the 11-16 Hz frequency region that exhibits chaos and/or quasi-periodic responses. Results are omitted for brevity, but for all six of the experimental configurations, the differences in the FRC are small. The contact-spring stiffness is increased to  $K_c = 7.0 * 10^4 N/m$  in Figure 7(b) and is five times the original value. The same of ICs is used for computation. It is immediately seen that the resonance peak has shifted up in frequency from 16 Hz to 25 Hz, and the rest of the response has shifted to higher frequency and lower amplitude. These results also show high similarity with and without event detection, with only minor differences at some forcing frequencies. The last FRC in Figure 7(c) is computed with  $K_c = 1.4 * 10^{10} N/m$ , which is one million times the first contact stiffness, and  $x_0 \in \{0, 0.1, 0.2, 0.4, 0.6, 0.8\} mm$ , to simulate hard impact. No resonance peak is visible anymore, even at higher frequencies, and instead the response amplitude is more uniform and limited in range. There are more frequency bands where chaos or multiple solutions are present compared to the lower-stiffness cases, but the results with and without event location still agree well in the periodic ranges.

Moving on to the bifurcation diagrams, the first one is in Figure 7(d) and shows the dependence on  $K_c$  at a forcing frequency of 5 Hz and  $x_0 = 0.32 mm$ . At the lowest values of contact stiffness, the response appears periodic and decreases in amplitude before encountering several successive bifurcations as  $K_c$  increases. Near the figure center, a structure in the middle of the response branches

out and persists until the solution becomes chaotic as  $K_c$  continues increasing. This structure seems to be birthed by a grazing bifurcation at  $K_c \approx 2.5 * 10^4 N/m$  with the lower freeplay boundary. The response converges on chaotic behavior beyond  $K_c > 5 * 10^6 N/m$ . Across the figure, results with and without event location agree well everywhere except one region near the grazing bifurcation where a narrow band of chaos is not captured without event location. Figure 7(e) shows the results for forcing frequency of 17 Hz and  $x_0 = 0.32 \text{ mm}$  and shows the system converges onto two different behaviors at soft (periodic) and hard (chaotic) contact stiffness. As  $K_c$  increases, the region between the limits appears to undergo a period-doubling bifurcation before abruptly hit a narrow band of chaos, which again abruptly changes to a high-amplitude period-1 response. A narrow band of nonlinear periodic behavior occurs near  $K_c \approx 3 * 10^5 N/m$ , and a region with the appearance of chaos occurs before the system transitions to persistent chaos above  $K_c > 2 * 10^7 N/m$ . Like before, the results with and without event location agree well except in a few areas, namely the chaos-like region in which some solutions are obtained only when using event location.

Lastly, Figure 7(f) shows the results for forcing frequency 23 Hz and  $x_0 = 0.32 \text{ mm}$ . The system again converges to two different behaviors at soft and hard contact stiffnesses. As  $K_c$  increases from soft to hard, the system starts off periodic and hits a region of nonlinear resonance before jumping to a significantly higher amplitude near  $K_c \approx 2 * 10^4 N/m$ . The amplitude quickly decreases before the system enters a complex region with many bifurcations leading to both periodic and chaotic solutions interspersed. The system then drops to a lower-amplitude periodic solution near  $K_c \approx 2 * 10^7 N/m$  and drops again to its converged periodic response shortly after. The differences with and without event location are more pronounced in this figure, and discrepancies occur in many places between the low- and high- $K_c$  limits. The responses without event location also appear to have a coarser texture than the responses with event location.

Based on the results of Figure 7, the main differences when using and neglecting accurate event location amount to either capturing different solutions or exhibiting a coarse, “poorly converged” appearance and occur primarily at intermediate levels of contact stiffness. The remainder of the analysis is now tailored to further study these results: the behavior near three different bifurcations is explored first with basins of attraction to reveal the different possible solutions and how event location affects which basin an arbitrary initial condition is attracted to. Next, the time histories, phase portraits, Poincaré maps, and Largest Lyapunov exponents of the different solutions/attractors are shown to study the effects of event location on the solutions themselves.

### 5.1 Influence of event location near a grazing bifurcation

Figure 8 shows the basins of attraction (BOAs), computed both with and without event location, near the dashed line in Figure 7(d) which corresponds to a grazing bifurcation as contact stiffness decreases. The BOAs in Figures 8(a, b) occur for  $K_c = 2.55 * 10^4 N/m$ ,  $\omega = 5 Hz$  and exhibit two different attractors each. Decreasing the stiffness to  $K_c = 2.32 * 10^4 N/m$  causes the grazing bifurcation and leads to Figures 8(c, d), which exhibits three attractors. The third attractor is only captured with event location and comprises just a few points at the bottom of Figure 8(c) in blue. Before the grazing bifurcation, the higher-amplitude solution is dominant while the second attractor exhibits a faint swirling behavior that is coarser but better seen without event location. After the grazing bifurcation, the two higher-amplitude solutions are roughly equal in dominance. A more pronounced swirling pattern is observed, and the basin boundaries for the result without event location are coarser than the result with event location. Based on the colormap, the highest-amplitude attractor also increased slightly in amplitude.

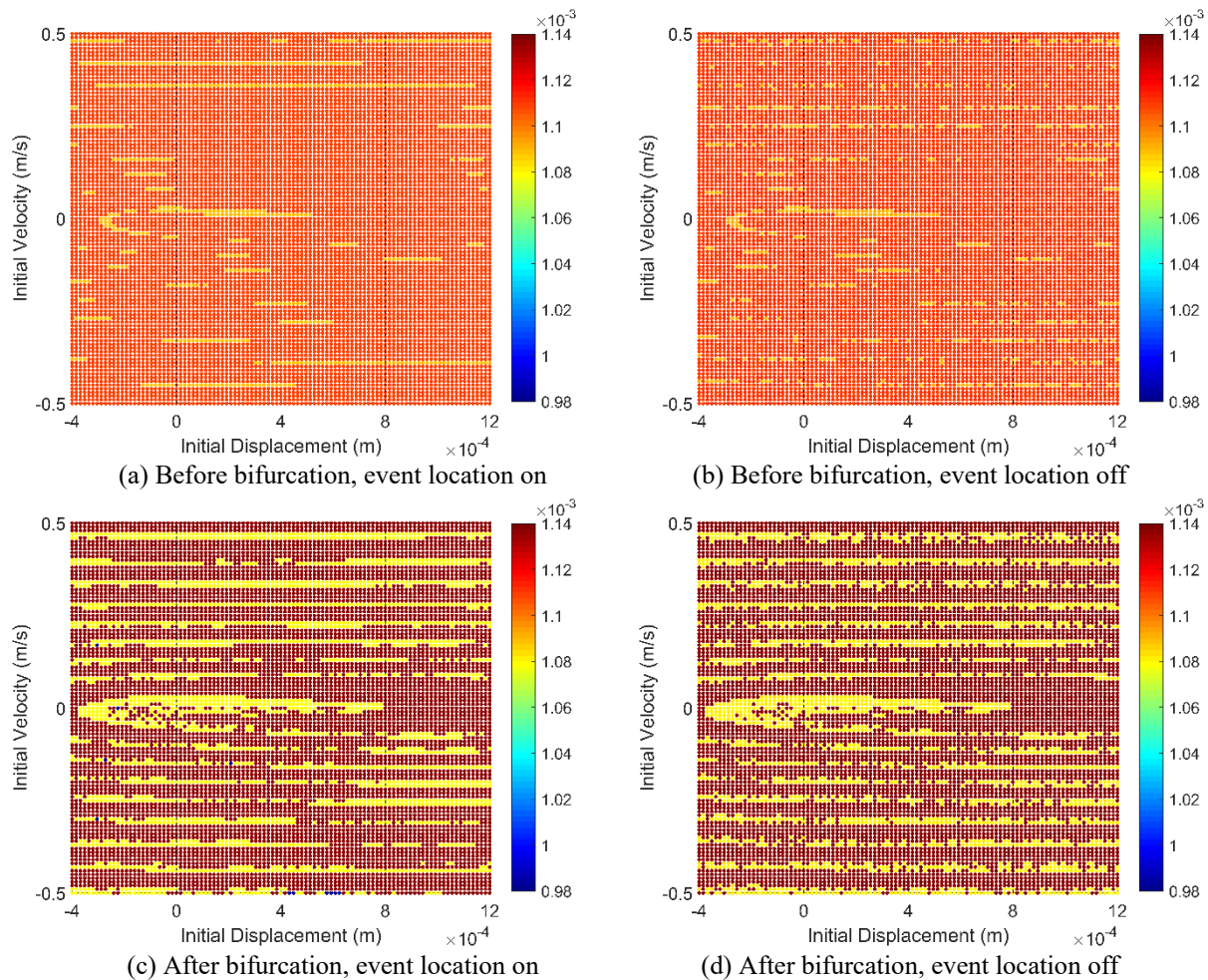


Fig. 8: Basins of attraction at  $\omega = 5 Hz$  both before (a, b,  $K_c = 2.55 * 10^4 N/m$ ) and after (c, d,  $K_c = 2.32 * 10^4 N/m$ ) the grazing bifurcation marked in Figure 7(d) as contact stiffness decreases. Plots (a, c) are computed with

event location, and plots (b, d) are computed without event location. Color corresponds to steady-state peak amplitude according to the colorbars and is used to distinguish the different possible responses. The black dashed lines denote the freeplay boundaries.

Figure 9 presents the time history, phase portrait, Poincaré map, and LLE for each attractor in Figures 8(a, b), both with and without event location. A grazing contact is seen for the first attractor, and the LLE in all cases is sufficiently close to zero as to conclude the responses are periodic. There is also excellent agreement between responses with and without event location. The solution data after the grazing bifurcation is presented in Figure 10, and it shows that grazing contact occurs for two attractors now. The LLE and Poincaré map indicate the responses are all period-1 still, and excellent agreement is still seen between attractors captured with and without event location. Attractor 3, however, was only captured when event location was used. A preliminary conclusion is that lack of accurate event location has a strong influence on what attractor a solution converges on, and possibly a lesser influence on the solution behavior of the attractor itself. This is supported by the zoomed inset in the upper-right plot of Figure 10: the results with and without event location differ on a small scale, with event location giving more refined results, but the differences are negligible on the whole scale of the response.

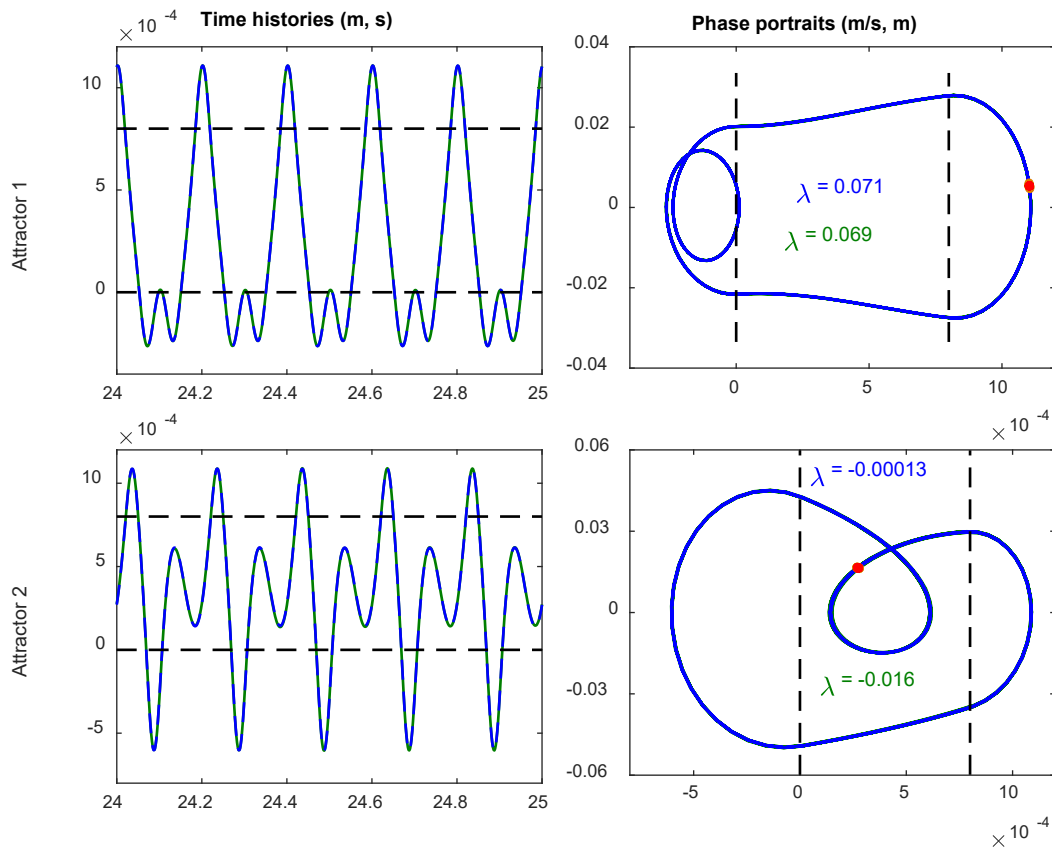


Fig. 9: Steady-state time histories and phase portraits/Poincaré maps of the attractors in Figures 8(a, b) for  $Kc = 2.55 * 10^4 N/m$ ,  $\omega = 5 Hz$ , before the grazing bifurcation. Green and orange indicates results obtained without event location, blue and red using event location.  $\lambda$  and its color denotes the corresponding response's largest Lyapunov exponent. Dashed lines denote freeplay boundaries.

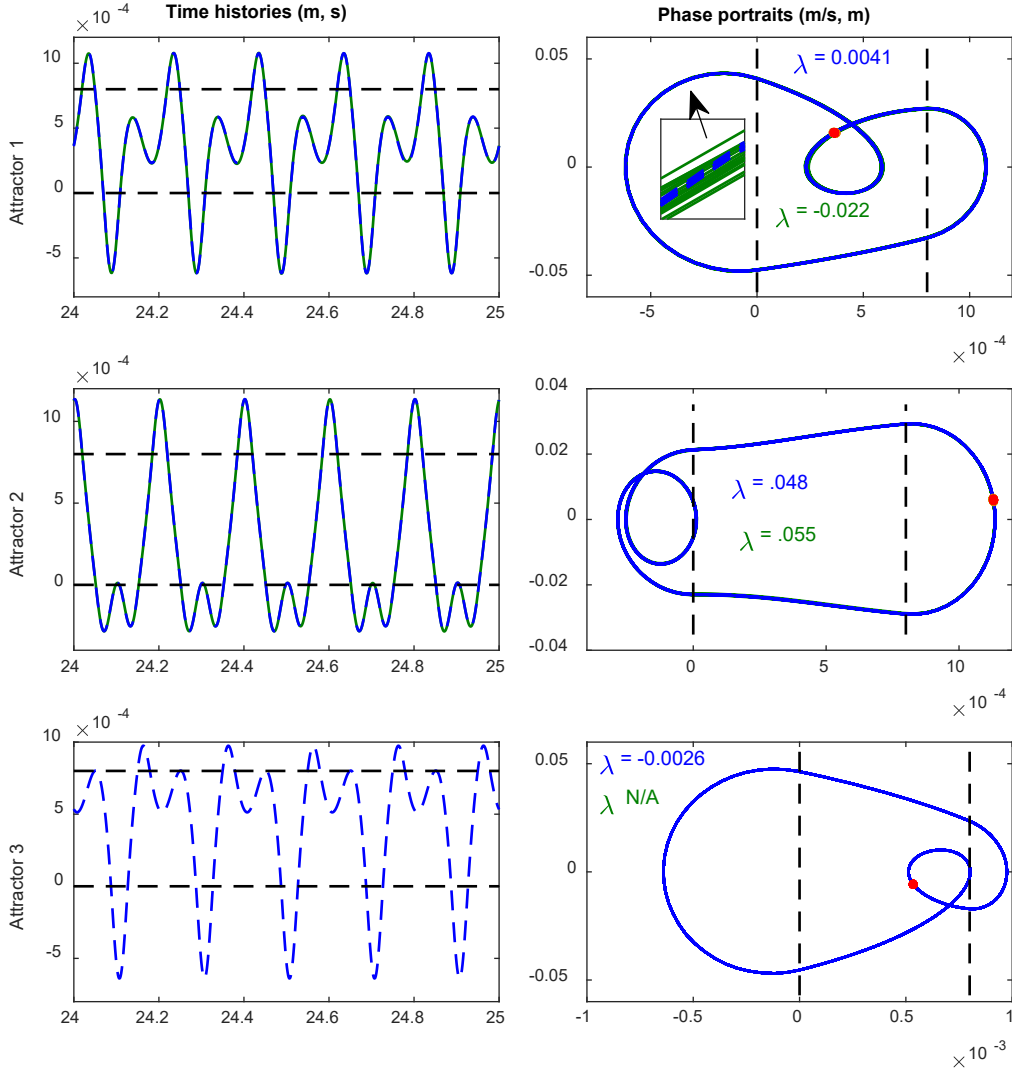


Fig. 10: Steady-state time histories and phase portraits/Poincaré maps of the attractors in Figures 7(c, d) for  $Kc = 2.32 * 10^4 N/m$ ,  $\omega = 5 Hz$ , after the grazing bifurcation. Green and orange indicates results obtained without event location, blue and red using event location.  $\lambda$  and its color denotes the corresponding response's largest Lyapunov exponent. Dashed lines denote freeplay boundaries.

## 5.2 Influence of event location near a period-doubling bifurcation

The next bifurcation studied occurs in Figure 7(e) near  $Kc = 8.0 * 10^3 N/m$ ,  $\omega = 17 Hz$  and will be seen to indicate a period-doubling bifurcation. Figure 11 shows the BOAs, computed both with and without event location, and both before and after the bifurcation. There exists only one attractor in Figures 11(a) and (b) before the bifurcation, and Figures 11(c) and (d) indicate that there is still only

one attractor after the bifurcation. Both sets of attractors with and without event location appear to have slightly different amplitudes, however, based on their respective colors.

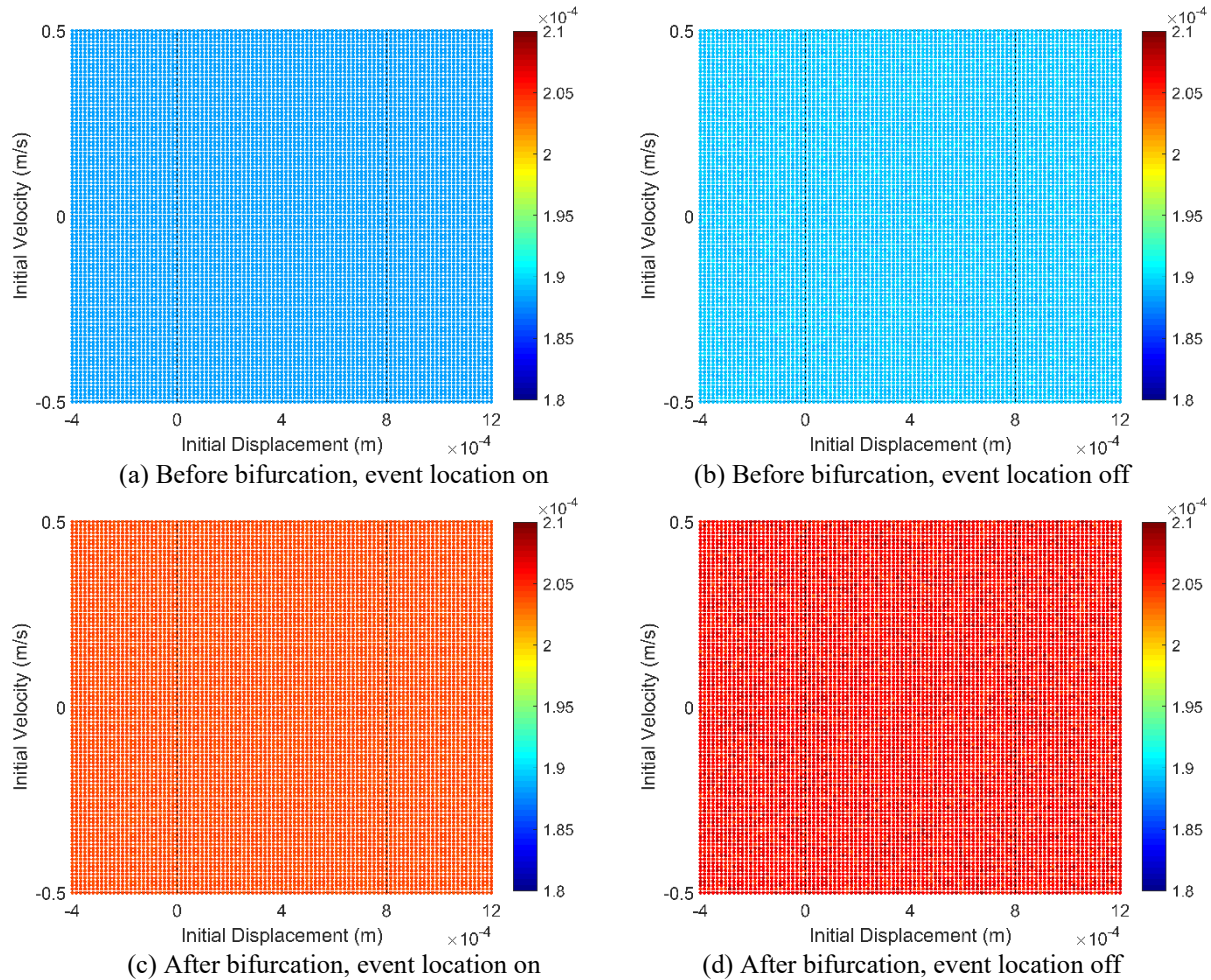


Fig. 11: Basins of attraction at  $\omega = 17 \text{ Hz}$  both before (a, b,  $K_c = 7,694 \text{ N/m}$ ) and after (c, d,  $K_c = 8,833 \text{ N/m}$ ) the period-doubling bifurcation marked in Figure 7(e). Plots (a, c) are computed with event location, and plots (b, d) are computed without event location. Color corresponds to steady-state peak amplitude according to the colorbars and is used to distinguish the different possible responses. The black dashed lines denote the freeplay boundaries.

Figure 12 presents the solution data for the attractors in Figures 11 both with and without event location and before and after the bifurcation. Comparing the results before and after the bifurcation now confirms that the attractor changes from a period-1 response to a period-2 response. Further, a near-grazing contact occurs in the period-2 response. The LLE in all four cases is small and supports the periodic nature of the responses. There is again excellent agreement between responses with and without event location.

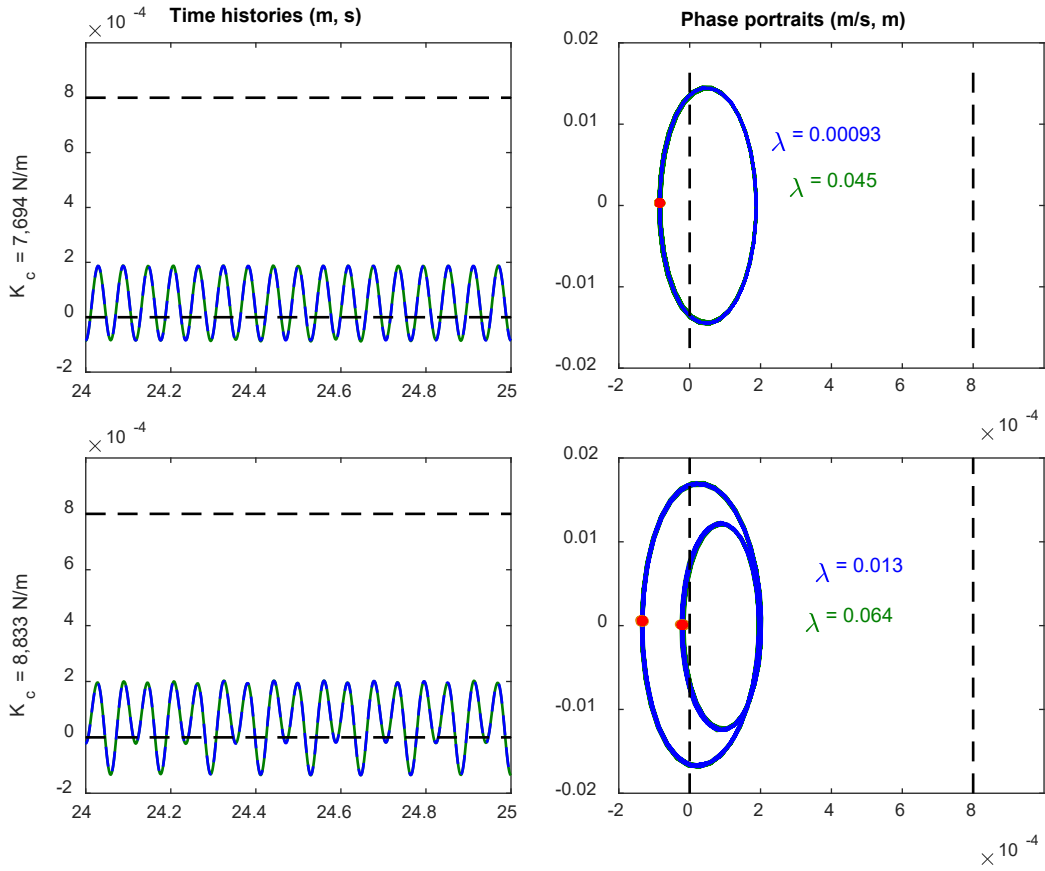


Fig. 12: Steady-state time histories and phase portraits/Poincaré maps of the attractors in Figure 11 at  $\omega = 17 \text{ Hz}$  before ( $K_c = 7,694 \text{ N/m}$ ) and after ( $K_c = 8,833 \text{ N/m}$ ) the period-doubling bifurcation. Green and orange indicates results obtained without event location, blue and red using event location.  $\lambda$  and its color denotes the corresponding response's largest Lyapunov exponent. Dashed lines denote freeplay boundaries.

### 5.3 Influence of event location near a transition to chaos

The final bifurcation used to study the effects of neglecting accurate event location is a transition to chaos, as denoted in Figure 7(f) near  $K_c \approx 2 * 10^7 \text{ N/m}$ ,  $\omega = 23 \text{ Hz}$ . The basins of attraction near this bifurcation are shown in Figure 13 and all appear similar in likeness. In all cases, the highest-amplitude attractor is dominant, and there were found to be four attractors in total. There appears to be no structure within the basin as seen previously, instead taking on a granular appearance throughout.

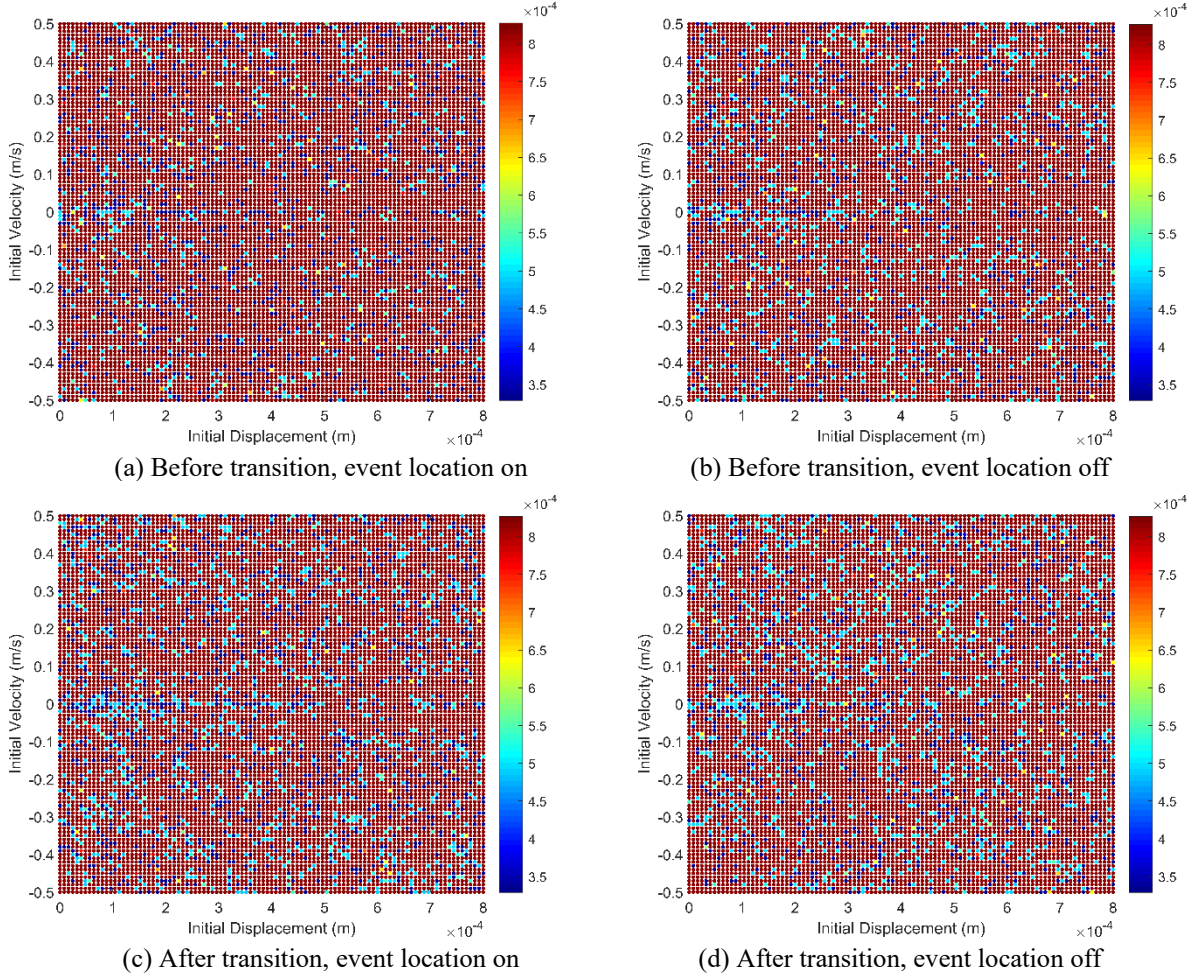


Fig. 13: Basins of attraction at  $\omega = 23 \text{ Hz}$  both before (a, b,  $K_c = 1.84 * 10^7 \text{ N/m}$ ) and after (c, d,  $K_c = 1.94 * 10^7 \text{ N/m}$ ) the transition to chaos marked in Figure 7(f). Plots (a, c) are computed with event location, and plots (b, d) are computed without event location. Color corresponds to steady-state peak amplitude according to the colorbars and is used to distinguish the different possible responses. The black dashed lines denote the freeplay boundaries.

Because the attractors appear the same both before and after the transition to chaos seen in Figure 7(f), it is inferred that the specific initial condition used to make the bifurcation diagram caused the system to simply converge onto a different attractor. Figure 14 therefore presents the solution data for all four attractors in Figure 13(a) both with and without event location. The first attractor oscillates between the upper and lower freeplay boundaries in a period-1 manner, although the Poincaré maps and LLEs indicate there is some level of coarseness or small instability to the motion. This is because the Poincaré map both with and without event location is smeared over a small area rather than a focused point, and the LLEs are no longer small enough to neglect. Interestingly, the response without event location has its Poincaré map covering a larger area but has a smaller LLE than the response with event location. Attractor 2 is a roughly period-3 response that also exhibits slightly unstable traits. The Poincaré map both with and without event location is smeared across three “points”, the LLE for both

is not negligibly small (and higher for the response without event location), and the time histories with and without event location are noticeably out of phase. Attractor 3 appears to be fully chaotic for the response with event location: the Poincaré map takes up a large area, and LLE is significantly large. The response without event location also appears chaotic, but to a smaller degree: The Poincaré map consists of five isolated “points”, and the LLE is of similar magnitude as those of attractors 1 and 2. Lastly, attractor 4 appears to be period-2 and has smaller LLEs than the previous attractors. The difference between responses with and without event location is a matter of coarseness.

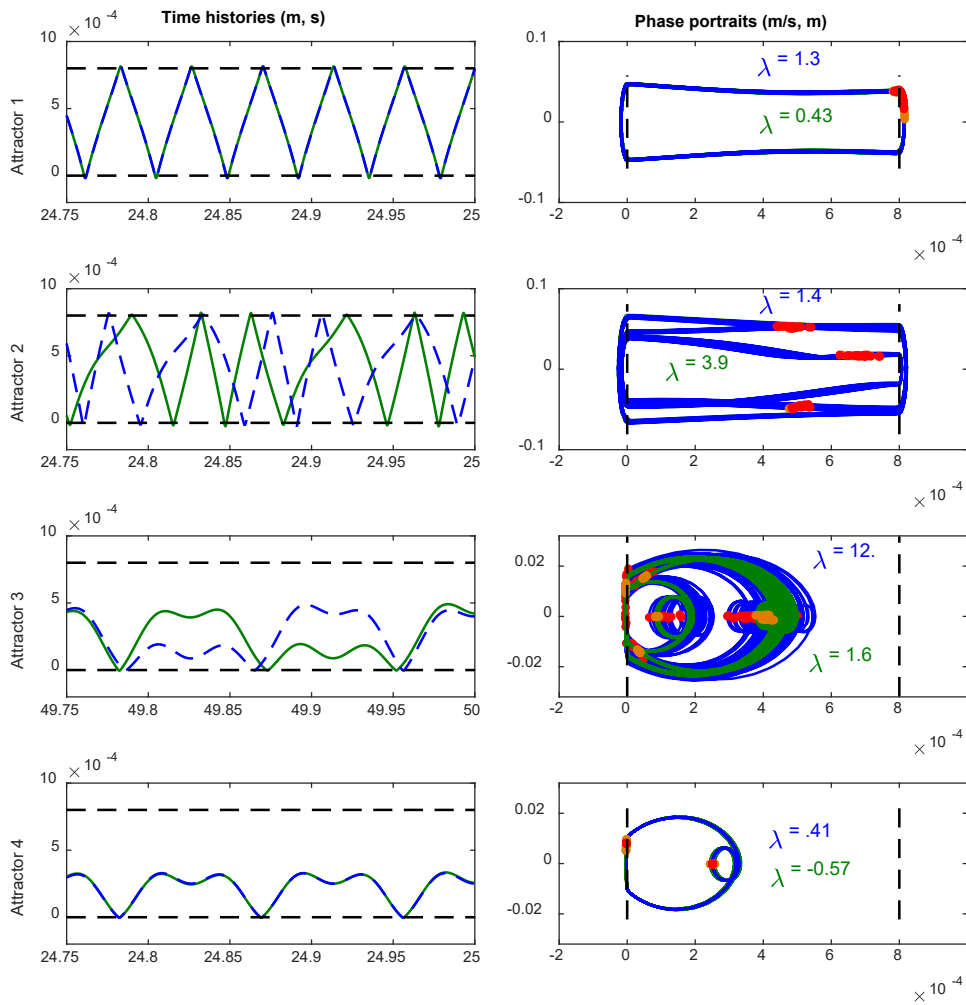


Fig. 14: Steady-state time histories and phase portraits/Poincaré maps of the attractors in Figure 13 at  $Kc = 1.84 * 10^7 N/m$ ,  $\omega = 23Hz$  corresponding to the observed transition to chaos. Green and orange indicates results obtained without event location, blue and red using event location.  $\lambda$  and its color denotes the corresponding response’s largest Lyapunov exponent. Dashed lines denote freeplay boundaries.

## 6 Conclusions

In the present study, the different types of behavior and inaccuracies that can occur when contact is not adequately accounted for in a piecewise-smooth dynamical system were studied as the strength

of the contact stiffness increases from soft contact to hard impact. A MATLAB<sup>®</sup>-based numerical method, based on the work of Wright et al.[62], was first validated against experimental data and showed good agreement with experimental results. Then, as the contact stiffness is increased towards hard impact, the numerical results have shown a few key behaviors in this system's response when computed with and without an event location procedure.

First is that the response without event location will be accurate if the contact stiffness is sufficiently small or large. For a small contact stiffness, the freeplay nonlinearity is weak; an improperly captured timestep near a contact boundary evidently will not cause a lot of accumulating error because, intuitively, the added contact stiffness does not change the system much. On the other hand, for a large contact stiffness, the freeplay nonlinearity is strong; hard contact tended to cause chaotic responses, so the error of an improperly captured timestep is likely swallowed up in chaos. Another factor that may be important is how the MATLAB<sup>®</sup> ode45 function has an adaptive timestep that can increase or decrease automatically. When a large contact stiffness is present, it would make sense if ode45 decreased the timestep to account for the large value, thereby reducing error. This would explain why the largest discrepancies were seen at intermediate values of contact stiffness.

The second key behavior is that neglecting event location has little effect on the behavior of the attractors themselves. In nearly all the time histories and phase portraits above, the solutions with and without event location corresponding to the same attractor agreed well, with the only difference being the results without event location looked coarser and "poorly converged" compared to the results with event location. Non-physical or otherwise fictitious responses were never formed, so the most severe danger for real-life design or experiments would be moving through a multistable region in which a high-amplitude or chaotic is not detected during simulation. If a subharmonic or other isolated resonance is not detected when modeling a new aircraft part, for example, then this allows the possibility of activating the high-amplitude response and causing severe damage.

On that note, the third key behavior is that the use or neglect of an event location procedure can affect the basin of attraction boundaries of the system. Results showed that basins of attraction computed without event location still produced the same attractors as basins computed with event location, with the same periodic or chaotic behavior. However, the basin boundaries can be changed when neglecting event location, often resulting in coarser boundaries. In a system that already exhibits multistability due to dependence on initial conditions, the inaccuracy of not capturing contact points adds to the difficulty of predicting what type of response the system will produce under a given set of system parameters. This has practical implications for modeling and validating experimental data of

contact systems: performing multiple test runs, starting from different initial conditions or subject to small perturbations, is important to ensure that all basins of attraction are found.

### **Acknowledgements**

B. E. Saunders, R. J. Kuether, and A. Abdelkefi acknowledge the financial support of the Laboratory Directed Research and Development program at Sandia National Laboratories, a multimission laboratory managed and operated by National Technology and Engineering Solutions of Sandia LLC, a wholly owned subsidiary of Honeywell International Inc. for the U.S. Department of Energy's National Nuclear Security Administration under contract DE-NA0003525. This paper describes objective technical results and analysis. Any subjective views or opinions that might be expressed in the paper do not necessarily represent the views of the U.S. Department of Energy or the United States Government.

R. Vasconcellos acknowledges the financial support of the Brazilian agencies CAPES (grant 88881.302889/2018-01) and CNPq (grant 311082/2016-5).

### **Compliance with ethical standards**

Conflict of interest: The authors declare that they have no conflict of interest.

### **References**

- [1] Thota, P., Zhao, X., and Dankowicz, H. (2006). Co-dimension-Two Grazing Bifurcations in Single-Degree-of-Freedom Impact Oscillators. *ASME Journal of Computational and Nonlinear Dynamics*, **1**(4), 328–335. Doi: <https://doi.org/10.1115/1.2338658>
- [2] Shan, Y., Jinchun, J., and Guilin, W. (2019). Complex near-grazing dynamics in impact oscillators. *International Journal of Mechanical Sciences*, **156**, 106-122. Doi: <https://doi.org/10.1016/j.ijmecsci.2019.03.023>
- [3] Lyu, X., Gao, Q., and Luo, G. (2020). Dynamic characteristics of a mechanical impact oscillator with a clearance. *International Journal of Mechanical Sciences*, **178**, 105605. Doi: <https://doi.org/10.1016/j.ijmecsci.2020.105605>
- [4] Fu, S., Liu, Y., and Chávez, J.P. (2020). Discontinuous Bifurcation of a Soft-Impact System. *International Journal of Bifurcation and Chaos*, **30**(9), p.2050132. Doi: <https://doi.org/10.1142/S0218127420501321>
- [5] Ing, J., Pavlovskaja, E., and Wiercigroch, M. (2011) Complex Nonlinear Response of a Piecewise Linear Oscillator: Experiment and Simulation. In Stépán G., Kovács L.L., Tóth A. (eds) *IUTAM Symposium on Dynamics Modeling and Interaction Control in Virtual and Real Environments*, IUTAM Bookseries, **30**, pp. 135-143. Springer, Dordrecht. Doi: [https://doi.org/10.1007/978-94-007-1643-8\\_16](https://doi.org/10.1007/978-94-007-1643-8_16)
- [6] Suda, N. and Banerjee, S. (2016). Why does narrow band chaos in impact oscillators disappear over a range of frequencies?. *Nonlinear Dynamics*, **86**, pp. 2017–2022. Doi: <https://doi.org/10.1007/s11071-016-3011-y>
- [7] Massi, F., Rocchi, J., Culla, A., and Berthier, Y. (2010). Coupling system dynamics and contact behaviour: Modelling bearings subjected to environmental induced vibrations and ‘false brinelling’

- degradation. *Mechanical Systems and Signal Processing*, **24**(4), 1068-1080. Doi: <https://doi.org/10.1016/j.ymssp.2009.09.004>
- [8] Dion, J. L., Le Moyne, S., Chevallier, G., and Sebbah, H. (2009). Gear impacts and idle gear noise: Experimental study and non-linear dynamic model. *Mechanical Systems and Signal Processing*, **23**(8), 2608-2628. Doi: <https://doi.org/10.1016/j.ymssp.2009.05.007>
- [9] Blazejczyk-Okolewska, B., Czolczynski, K., and Kapitaniak, T. (2010). Hard versus soft impacts in oscillatory systems modeling. *Communications in Nonlinear Science and Numerical Simulation*, **15**(5), pp. 1358-1367. Doi: <https://doi.org/10.1016/j.cnsns.2009.05.046>
- [10] Bazhenov, V.A., Pogorelova, O.S., and Postnikova, T.G. (2013). Comparison of Two Impact Simulation Methods Used for Nonlinear Vibroimpact Systems with Rigid and Soft Impacts. *Journal of Nonlinear Dynamics*, **2013**, Article ID 485676. Doi: <https://doi.org/10.1155/2013/485676>
- [11] Wang, J., Yang, J., & Li, Q. (2018). Quasi-static analysis of the nonlinear behavior of a railway vehicle gear system considering time-varying and stochastic excitation. *Nonlinear Dynamics*, **93**, 463-485. Doi: <https://doi.org/10.1007/s11071-018-4204-3>
- [12] Yang, Y., Xia, W., Han, J., Song, Y., Wang, J., & Dai, Y. (2019). Vibration analysis for tooth crack detection in a spur gear system with clearance nonlinearity. *International Journal of Mechanical Sciences*, **157–158**, pp. 648-661. Doi: <https://doi.org/10.1016/j.ijmecsci.2019.05.012>
- [13] Geng, Z., Xiao, K., Wang, J., & Li, J. (2019). Investigation on nonlinear dynamic characteristics of a new rigid-flexible gear transmission with wear. *Journal of Vibration and Acoustics*, **141**(5), 051008. Doi: <https://doi.org/10.1115/1.4043543>
- [14] Chen, Q., Wang, Y., Tian, W., Wu, Y., & Chen, Y. (2019). An improved nonlinear dynamic model of gear pair with tooth surface microscopic features. *Nonlinear Dynamics*, **96**, 1615-1634. Doi: <https://doi.org/10.1007/s11071-019-04874-1>
- [15] Chung, K.W., Chan, C.L., & Lee, B.H.K. (2007). Bifurcation analysis of a two-degree-of-freedom aeroelastic system with freeplay structural nonlinearity by a perturbation-incremental method. *Journal of Sound and Vibration*, **299**(3), 520-539. Doi: <https://doi.org/10.1016/j.jsv.2006.06.059>
- [16] Abdelkefi, A., Vasconcellos, R., Marques, F.D., & Hajj, M.R. (2012). Modeling and identification of freeplay nonlinearity. *Journal of Sound and Vibration*, **331**(8), 1898-1907. Doi: <https://doi.org/10.1016/j.jsv.2011.12.021>
- [17] Vasconcellos, R., Abdelkefi, A., Marques, F.D., & Hajj, M.R. (2012). Representation and analysis of control surface freeplay nonlinearity. *Journal of Fluids and Structures*, **31**, 79–91. Doi: <https://doi.org/10.1016/j.jfluidstructs.2012.02.003>
- [18] Vasconcellos, R., Abdelkefi, A., Hajj, M.R., & Marques, F.D. (2014). Grazing bifurcation in aeroelastic systems with freeplay nonlinearity. *Communications in Nonlinear Science and Numerical Simulation*, **19**(5), 1611-1625. Doi: <https://doi.org/10.1016/j.cnsns.2013.09.022>
- [19] Dai, H., Yue, X., Xie, D., and Atluri, S. N. (2014). Chaos and chaotic transients in an aeroelastic system. *Journal of Sound and Vibration*, **333**(26), 7267-7285. Doi: <https://doi.org/10.1016/j.jsv.2014.08.034>
- [20] Dai, H., Yue, X., Yuan, J., Xie, D., & Atluri, S.N. (2015). A comparison of classical Runge-Kutta and Henon's methods for capturing chaos and chaotic transients in an aeroelastic system with freeplay nonlinearity. *Nonlinear Dynamics*, **81**, 169–188. Doi: <https://doi.org/10.1007/s11071-015-1980-x>
- [21] Vasconcellos, R. & Abdelkefi, A. (2015). Nonlinear dynamical analysis of an aeroelastic system with multi-segmented moment in the pitch degree-of-freedom. *Communications in Nonlinear Science and Numerical Simulation*, **20**(1), 324-334. Doi: <https://doi.org/10.1016/j.cnsns.2014.05.017>
- [22] Cai, Y. & Chen, S.S. (1992). Chaotic vibrations of nonlinearly supported tubes in crossflow. *ASME Journal of Pressure Vessel Technology*, **115**(2), 128–134. Doi: <https://doi.org/10.1115/1.2929506>
- [23] Ibrahim, R.A. (2010). Overview of mechanics of pipes conveying fluids—part i: fundamental studies. *Journal of Pressure Vessel Technology*, **132**(3), 034001. Doi: <https://doi.org/10.1115/1.4001271>

- [24] Wang, L., Liu, Z.Y., Abdelkefi, A., Wang, Y.K., & Dai, H.L. (2017). Nonlinear dynamics of cantilevered pipes conveying fluid: Towards a further understanding of the effect of loose constraints. *International Journal of Non-Linear Mechanics*, **95**, 19–29. Doi: <https://doi.org/10.1016/j.ijnonlinmec.2017.05.012>
- [25] Andreaus, U. and De Angelis, M. (2016). Nonlinear dynamic response of a base-excited SDOF oscillator with double-side unilateral constraints. *Nonlinear Dynamics*, **84**, pp. 1447–1467. Doi: <https://doi.org/10.1007/s11071-015-2581-4>
- [26] Andreaus, U., Baragatti, P., De Angelis, M., and Perno, S. (2017). A Preliminary Experimental Study About Two-Sided Impacting SDOF Oscillator Under Harmonic Excitation. *ASME Journal of Computational and Nonlinear Dynamics*, **12**(6), 061010. Doi: <https://doi.org/10.1115/1.4036816>
- [27] Christopher, P.J., Dobson, B., and Alexander, N.A. (2020). Exploring the Dynamics of Base-Excited Structures Impacting a Rigid Stop. *Mathematical Problems in Engineering*, **2020**, Article ID 6721025. Doi: <https://doi.org/10.1155/2020/6721025>
- [28] Fan, J., Gao, M., and Chen, S. (2021). Discontinuous Dynamic Analysis of a Class of 2-DOF Oscillators With Strong Nonlinearity Under a Periodic Excitation. *IEEE Access*, **9**, pp. 77997-78016. Doi: <https://doi.org/10.1109/ACCESS.2021.3083809>
- [29] Nguyen, V.D., Duong, T.H., Chu, N.H., and Ngo, Q.H. (2017). The effect of inertial mass and excitation frequency on a Duffing vibro-impact drifting system. *International Journal of Mechanical Sciences*, **124-125**, 9-21. Doi: <https://doi.org/10.1016/j.ijmecsci.2017.02.023>
- [30] Sayah, M., Baptista, M.S., Ing, J., and Wiercigroch, M. (2015). Attractor reconstruction of an impact oscillator for parameter identification. *International Journal of Mechanical Sciences*, **103**, 212-223. Doi: <https://doi.org/10.1016/j.ijmecsci.2015.08.005>
- [31] Brzeski, P., Pavlovskaja, E., Kapitaniak, T., and Perlikowski, P. (2017). Controlling multistability in coupled systems with soft impacts. *International Journal of Mechanical Sciences*, **127**, 118-129. Doi: <https://doi.org/10.1016/j.ijmecsci.2016.12.022>
- [32] Pilipchuk, V. N. (1996). Analytical study of vibrating systems with strong non-linearities by employing saw-tooth time transformations. *Journal of Sound and Vibration*, **192**(1), 43–64. Doi: <https://doi.org/10.1006/jsvi.1996.0175>
- [33] Mikhlin, Y.V. and Reshetnikova, S.N. (2005). Dynamical interaction of an elastic system and a vibro-impact absorber. *Mathematical Problems in Engineering*, **2006**, Article ID 037980. Doi: <https://doi.org/10.1155/MPE/2006/37980>
- [34] Avramov, K. V. and Borysiuk, O. V. (2008). Analysis of an impact Duffing oscillator by means of a nonsmooth unfolding transformation. *Journal of Sound and Vibration*, **318**(4-5), 1197-1209. Doi: <https://doi.org/10.1016/j.jsv.2008.05.005>
- [35] Pilipchuk, V.N. (2015). Closed-form solutions for oscillators with inelastic impacts. *Journal of Sound and Vibration*, **359**, pp. 154-167. Doi: <https://doi.org/10.1016/j.jsv.2015.08.023>
- [36] Pilipchuk, V.N. (2019). Non-smooth Spatial and Temporal Substitutions in Impact Dynamics. In: Andrianov, I., Manevich, A., Mikhlin, Y., and Gendelman, O. (eds) *Problems of Nonlinear Mechanics and Physics of Materials*. *Advanced Structured Materials*, **94**. Springer, Cham. Doi: [https://doi.org/10.1007/978-3-319-92234-8\\_8](https://doi.org/10.1007/978-3-319-92234-8_8)
- [37] Nordmark, A.B. (1991). Non-periodic motion caused by grazing incidence in an impact oscillator. *Journal of Sound and Vibration*, **145**(2), pp. 279-297. Doi: [https://doi.org/10.1016/0022-460X\(91\)90592-8](https://doi.org/10.1016/0022-460X(91)90592-8)
- [38] Nordmark, A.B. (1997). Universal limit mapping in grazing bifurcations. *Physical Review E*, **55**(1), pp. 266-270. Doi: <https://doi.org/10.1103/PhysRevE.55.266>
- [39] Molenaar, J., de Weger, J. G., and van de Water, W. (2001). Mappings of grazing-impact oscillators. *Nonlinearity*, **14**(2), pp. 301-321. Doi: <https://doi.org/10.1088/0951-7715/14/2/307>

- [40] Ma, Y., Ing, J., Banerjee, S., Wiercigroch, M., and Pavlovskaja, E. (2008). The nature of the normal form map for soft impacting systems. *International Journal of Non-Linear Mechanics*, **43**(6), pp. 504-513. Doi: <https://doi.org/10.1016/j.ijnonlinmec.2008.04.001>
- [41] Andreaus, G., Placidi, L., and Rega, G. (2010). Numerical simulation of the soft contact dynamics of an impacting bilinear oscillator. *Communications in Nonlinear Science and Numerical Simulation*, **15**(9), pp. 2603-2616. Doi: <https://doi.org/10.1016/j.cnsns.2009.10.015>
- [42] Simpson, D.J.W., Avrutin, V., and Banerjee, S. (2020). Nordmark map and the problem of large-amplitude chaos in impact oscillators. *Physical Review E*, **102**, 022211. Doi: <https://doi.org/10.1103/PhysRevE.102.022211>
- [43] Kuether, R.J., Renson, L., Detroux, T., Grappasonni, C., Kerschen, G., & Allen, M.S. (2015). Nonlinear normal modes, modal interactions and isolated resonance curves. *Journal of Sound and Vibration*, **351**, 299-310. Doi: <https://doi.org/10.1016/j.jsv.2015.04.035>
- [44] Peter, S., Schreyer, F., and Leine, R. I. (2019). A method for numerical and experimental nonlinear modal analysis of nonsmooth systems. *Mechanical Systems and Signal Processing*, **120**, 793-807. Doi: <https://doi.org/10.1016/j.ymssp.2018.11.009>
- [45] Renson, L., Kerschen, G., and Cochelin, B. (2016). Numerical computation of nonlinear normal modes in mechanical engineering. *Journal of Sound and Vibration*, **364**, pp. 177-206. Doi: <https://doi.org/10.1016/j.jsv.2015.09.033>
- [46] Detroux, T., Renson, L., Masset, L., & Kerschen, G. (2015). The harmonic balance method for bifurcation analysis of large-scale nonlinear mechanical systems. *Computer Methods in Applied Mechanics and Engineering*, **296**, 18-38. Doi: <https://doi.org/10.1016/j.cma.2015.07.017>
- [47] Alcorta, R., Bague, S., Prabel, B., Piteau, P., & Jacquet-Richardet, G. (2019). Period doubling bifurcation analysis and isolated sub-harmonic resonances in an oscillator with asymmetric clearances. *Nonlinear Dynamics*, **98**, 2939–2960. Doi: <https://doi.org/10.1007/s11071-019-05245-6>
- [48] Saunders, B.E., Vasconcellos, R. Kuether, R.J., and Abdelkefi, A. (2021). Insights on the continuous representation of piecewise-smooth nonlinear systems: limits of applicability and effectiveness. *Nonlinear Dynamics*. Doi: <https://doi.org/10.1007/s11071-021-06436-w>
- [49] Brandão, A., Souza de Paula, A., Savi, M.A., and Thouverez, F. (2017). Nonlinear Dynamics and Chaos of a Nonsmooth Rotor-Stator System. *Mathematical Problems in Engineering*, **2017**, Article ID 8478951. Doi: <https://doi.org/10.1155/2017/8478951>
- [50] Henon, M. (1982). On the numerical computation of Poincaré maps. *Physica D: Nonlinear Phenomena*, **5**(2-3), 412-414. Doi: [https://doi.org/10.1016/0167-2789\(82\)90034-3](https://doi.org/10.1016/0167-2789(82)90034-3)
- [51] Conner, M. D., Virgin, L. N., & Dowell, E. H. (1996). Accurate numerical integration of state-space models for aeroelastic systems with free play. *AIAA Journal*, **34**(10), 2202-2205. Doi: <https://doi.org/10.2514/3.13377>
- [52] Wayhs-Lopes, L.D., Dowell, E.H., & Bueno, D.D. (2020). Influence of friction and asymmetric freeplay on the limit cycle oscillation in aeroelastic system: An extended Hénon's technique to temporal integration," *Journal of Fluids and Structures*, **96**, 103054. Doi: <https://doi.org/10.1016/j.jfluidstructs.2020.103054>
- [53] Doedel, E.J., Champneys, A.R., Fairgrieve, T.F., Kuznetsov, Y.A., Oldeman, B., Paffenroth, R., Sandstede, B., Wang, X., and Zhang, C. (2007). AUTO-07P: Continuation and bifurcation software for ordinary differential equations. <http://www.macs.hw.ac.uk/~gabriel/auto07/auto.html>
- [54] Dhooge, A., Govaerts, W., Kuznetsov, Y.A., Meijer, H.G.E., and Sautois, B. (2008). New features of the software MatCont for bifurcation analysis of dynamical systems. *Mathematical and Computer Modelling of Dynamical Systems*, **14**(2), pp. 147-175. Doi: <https://doi.org/10.1080/13873950701742754>
- [55] Dankowicz, H., Schilder, F.: *Recipes for Continuation*. Society for Industrial and Applied Mathematics, Philadelphia (2013).

- [56] Guillot, L., Cochelin, B., and Vergez, C. (2019). A Taylor series-based continuation method for solutions of dynamical systems. *Nonlinear Dynamics*, **98**, pp. 2827–2845. Doi: <https://doi.org/10.1007/s11071-019-04989-5>
- [57] Chong, A.S.E., Yue, Y., Pavlovskaja, E., and Wiercigroch, M. (2017). Global dynamics of a harmonically excited oscillator with a play: Numerical studies. *International Journal of Non-Linear Mechanics*, **94**, pp. 98-108. Doi: <https://doi.org/10.1016/j.ijnonlinmec.2017.03.015>
- [58] Shampine, L.F. & Thompson, S. (2000). Event location for ordinary differential equations. *Computers & Mathematics with Applications*, **39**(5-6), 43-54. Doi: [https://doi.org/10.1016/S0898-1221\(00\)00045-6](https://doi.org/10.1016/S0898-1221(00)00045-6)
- [59] Jiang, H., Chong, A.S.E., Ueda, Y., and Wiercigroch, M. (2017). Grazing-induced bifurcations in impact oscillators with elastic and rigid constraints. *International Journal of Mechanical Sciences*, **127**, pp. 204-214. Doi: <https://doi.org/10.1016/j.ijmecsci.2017.02.001>
- [60] Calvo, M., Montijano, J.I., and Rande, L. (2008). The numerical solution of discontinuous IVPs by Runge–Kutta codes: a review. *Boletín de la Sociedad Española Matemática Aplicada*, **44**, pp. 33–53.
- [61] Calvo, M., Montijano, J.I., and Rande, L. (2016). Algorithm 968: DISODE45: A Matlab Runge-Kutta Solver for Piecewise Smooth IVPs of Filippov Type. *ACM Transactions on Mathematical Software*, **43**(3), Article 25. Doi: <https://dx.doi.org/10.1145/2907054>
- [62] Wright, J.P. and Pei, J-S. (2012). Solving Dynamical Systems Involving Piecewise Restoring Force Using State Event Location. *Journal of Engineering Mechanics*, **138**(8), 997-1020. Doi: [https://doi.org/10.1061/\(ASCE\)EM.1943-7889.0000404](https://doi.org/10.1061/(ASCE)EM.1943-7889.0000404)
- [63] Dallas, S., Machairas, K., and Papadopoulos, E. (2017). A Comparison of Ordinary Differential Equation Solvers for Dynamical Systems with Impacts. *ASME Journal of Computational and Nonlinear Dynamics*, **12**(6), 061016. Doi: <https://doi.org/10.1115/1.4037074>
- [64] Frumusa, M. & Vaccaro, V. (2019). Investigation on the Effects of Control Surface Freeplay on the Aeroelastic Characteristics of a Trainer Aircraft and Extension of Limits in Support of Maintenance Tasks. *International Forum on Aeroelasticity and Structural Dynamics (IFASD 2019)*, June 9-13, Savannah, Georgia, USA.
- [65] Wolf, A., Swift, J.B., Swinney, H.L., and Vastano, J.A. (1985). Determining Lyapunov Exponents from a Time Series. *Physica D*, **16**(3), pp. 285-317. Doi: [https://doi.org/10.1016/0167-2789\(85\)90011-9s](https://doi.org/10.1016/0167-2789(85)90011-9s)
- [66] de Langre, E. & Lebreton, G. (1996). An experimental and numerical analysis of chaotic motion in vibration with impact. *ASME 8th International Conference on Pressure Vessel Technology*, July 21-26, Montreal, Quebec, Canada.
- [67] Moler, C.B. (1997). Are we there yet? Zero crossing and event handling for differential equations. *Matlab News & Notes*, 16–17. <https://www.mathworks.com/company/newsletters/articles/are-we-there-yet-zero-crossing-and-event-handling-for-differential-equations.html>
- [68] Marzouk, O. A., Nayfeh, A. H. (2010). Characterization of the flow over a cylinder moving harmonically in the cross-flow direction. *International Journal of Non-Linear Mechanics*, **45**, 821-833. Doi: <https://doi.org/10.1016/j.ijnonlinmec.2010.06.004>
- [69] Sprott, J.C. and Xiong, A. (2015). Classifying and quantifying basins of attraction. *Chaos: An Interdisciplinary Journal of Nonlinear Science*, **25**, 083101. Doi: <https://doi.org/10.1063/1.4927643>